Multi-frequency observations of SGR J1935+2154

M. Bailes, C.G. Bassa, G. Bernardi, S. Buchner, M. Burgay, M. Caleb, A.J. Cooper, G. Desvignes, P.J. Groot, I. Heywood, et al.

Monthly Notices
of the
ROYAL ASTRONOMICAL SOCIETY

MNRAS **503,** 5367–5384 (2021)
Advance Access publication 2021 March 17

doi:10.1093/mnras/stab749

Multifrequency observations of SGR J1935+2154

M. Bailes,[1,2] C. G. Bassa,[3] G. Bernardi,[4,5,6] S. Buchner,[6] M. Burgay,[7] M. Caleb,[8] A. J. Cooper,[3,9] G. Desvignes,[10,11] P. J. Groot,[12,13,14] I. Heywood,[5,6,15] F. Jankowski,[8] R. Karuppusamy,[10] M. Kramer,[8,10] M. Malenta,[8] G. Naldi,[4] M. Pilia,[7] G. Pupillo,[4] K. M. Rajwade,[8] L. Spitler,[10] M. Surnis,[8] B. W. Stappers,[8]★ A. Addis,[16] S. Bloemen,[12] M. C. Bezuidenhout,[8] G. Bianchi,[4] D. J. Champion,[10] W. Chen,[10] L. N. Driessen,[8] M. Geyer,[6] K. Gourdji,[9] J. W. T. Hessels,[3,9] V. I. Kondratiev,[3,17] M. Klein-Wolt,[12] E. Körding,[12] R. Le Poole,[18] K. Liu,[10] M. E. Lower,[1,2,19] A. G. Lyne,[8] A. Magro,[20] V. McBride,[21] M. B. Mickaliger,[8] V. Morello,[8] A. Parthasarathy,[10] K. Paterson,[22] B. B. P. Perera,[23] D. L. A. Pieterse,[12] Z. Pleunis,[24,25] A. Possenti,[7,26] A. Rowlinson,[3,9] M. Serylak,[6] G. Setti,[4,27] M. Tavani,[28,29] R. A. M. J. Wijers,[9] S. ter Veen,[3] V. Venkatraman Krishnan,[10] P. Vreeswijk[12] and P. A. Woudt[13]

Affiliations are listed at the end of the paper

Accepted 2021 March 5. Received 2021 March 5; in original form 2020 December 23

ABSTRACT

Magnetars are a promising candidate for the origin of fast radio bursts (FRBs). The detection of an extremely luminous radio burst from the Galactic magnetar SGR J1935+2154 on 2020 April 28 added credence to this hypothesis. We report on simultaneous and non-simultaneous observing campaigns using the Arecibo, Effelsberg, LOFAR, MeerKAT, MK2, and Northern Cross radio telescopes and the MeerLICHT optical telescope in the days and months after the April 28 event. We did not detect any significant single radio pulses down to fluence limits between 25 mJy ms and 18 Jy ms. Some observing epochs overlapped with times when X-ray bursts were detected. Radio images made on 4 d using the MeerKAT telescope revealed no point-like persistent or transient emission at the location of the magnetar. No transient or persistent optical emission was detected over seven days. Using the multicolour MeerLICHT images combined with relations between DM, $N_{\rm H}$, and reddening, we constrain the distance to SGR J1935+2154, to be between 1.5 and 6.5 kpc. The upper limit is consistent with some other distance indicators and suggests that the April 28 burst is closer to two orders of magnitude less energetic than the least energetic FRBs. The lack of single-pulse radio detections shows that the single pulses detected over a range of fluences are either rare, or highly clustered, or both. It may also indicate that the magnetar lies somewhere between being radio-quiet and radio-loud in terms of its ability to produce radio emission efficiently.

Key words: stars: magnetars – fast radio bursts.

1 INTRODUCTION

Magnetars are possibly the most exotic objects of all the classes of neutron stars. High magnetic fields ($\gtrsim 10^{14}$ G) and intense X-ray/soft γ-ray emission combined with erratic spin-down behaviour makes them unique amongst the neutron star population. The soft gamma-ray repeater (SGR) J1935+2154 was discovered when the *Swift*-Burst Alert Telescope detected an X-ray burst on 2014 July 5 (Lien et al. 2014; Stamatikos et al. 2014). This initial burst was then followed by a number of other short bursts (Cummings 2014). Following this, the sky location of SGR J1935+2154 was quickly recognized to place it coincident with the supernova remnant (SNR) G57.2+0.8, strongly suggesting an association (Gaensler 2014). Follow-up radio observations with the Very Large Array (VLA) at 6 GHz revealed no persistent radio emission down to 41 μJy (3σ; Fong & Berger 2014). Subsequent observations with the Chandra X-ray telescope detected X-ray pulsations with a period of 3.24 s (Israel et al. 2014). Searches with the Giant Metrewave Radio Telescope (GMRT), Ooty, and Parkes telescopes failed to detect any pulsed radio emission (Burgay et al. 2014; Surnis et al. 2014). Since the initial X-ray outburst the source has undergone further outbursts in 2015 February, 2016 May, and 2019 November. It is noteworthy that sporadic X-ray bursts are seen (Kozlova et al. 2016; Younes et al. 2017a) even between these periods of activity, making it one of the most active magnetars known (Lin et al. 2020b). As well as the single pulse and periodicity searches, searches for continuum radio emission, which might be associated with a new pulsar wind nebula activated by the bursting activity, were carried out just after the discovery of the source, with the GMRT (Surnis et al. 2016). They report 3σ upper limits of 1.2 and 4.5 mJy at frequencies of 362.5 and 610 MHz, respectively. Searches for continuum emission associated

★ E-mail: Ben.Stappers@manchester.ac.uk

Table 1. Continuum observations of SGR J1935+2154, including their durations, where available.

Telescope	Date (UTC)	Duration (h)	$F_{\rm centre}$ (MHz)	BW (MHz)	Flux density (mJy)	References
EVN	2020 May 13	5.7	1670	128	0.016	Nimmo et al. (2020)
MWA	2020 May 3	4	154	31	14.4	An et al. (2020)
MWA	2020 May 4	4	185	31	3.8	An et al. (2020)
uGMRT	2020 May 27	3	650	200	0.090/0.060	Surnis et al. (2020a), Bera et al. (2020)
uGMRT	2020 May 28	3	1360	200	0.054/0.078	Surnis et al. (2020a), Bera et al. (2020)
uGMRT	2020 Jun 8	2	400	200	0.465	Surnis et al. (2020b)
VLA	2020 Apr 29	–	6000	4000	0.015	Ravi, Hallinan & Law (2020a)
VLA	2020 Apr 29	–	22 000	8000	0.018	Ravi et al. (2020a)
VLA	2020 Apr 30	–	6000	4000	0.007	Ravi, Hallinan & Law (2020b)
VLA	2020 Apr 30	–	22 000	8000	0.024	Ravi et al. (2020b)
GMRT	2014 Jul 14	1.25	610	33	1.2	Surnis et al. (2016)
VLA	2014 Jul 6	1	6000	4000	0.041	Fong & Berger (2014)

Note. The central frequency and bandwidth of the observations are indicated by $F_{\rm centre}$ and BW, respectively.

with this most recent burst have been undertaken by a wide range of telescopes and we summarize these in Table 1. In spite of deep searches, no continuum emission has been detected at the best known position of SGR J1935+2154. A detection of pulsar-wind nebula emission from the magnetar would have significant implications on the emission physics of the magnetar and its association with G57.2+0.8, although a pulsar-wind nebula has been detected around only one magnetar to date (Younes et al. 2016).

SGR J1935+2154 became active again from 2020 April 27 when multiple bursts were detected with a number of high-energy telescopes (e.g. Hurley et al. 2020; Palmer 2020; Younes et al. 2020b). On 2020 April 28, a very bright serendipitous radio burst, initially thought to be about a kJy ms in fluence, was detected by the Canadian Hydrogen Intensity Mapping Experiment (CHIME) telescope in a far sidelobe, but at a location that was consistent with the position of SGR J1935+2154 with a dispersion measure (DM) of 332.8 pc cm^{-3} (Scholz & CHIME/FRB Collaboration 2020). The burst was also independently detected by the Survey for Transient Astronomical Radio Emission 2 (STARE2) radio telescope (Bochenek et al. 2020b) with a reported fluence greater than 1.5 MJy ms and a very similar DM of 333.2 $\pm$ 0.8 pc cm^{-3}. Subsequently, a targeted observation of SGR J1935+2154 by the Five-hundred-metre Aperture Spherical Telescope (FAST) in China resulted in the detection of a fainter $\sim$30 mJy, highly polarized radio burst (Zhang et al. 2020b), indicating that it may be transitioning to a radio-loud magnetar state. The bright radio burst detected with CHIME in their 400–800 MHz band exhibits two components separated by 28.91 $\pm$ 0.02 ms (The CHIME/FRB Collaboration et al. 2020). They show very different spectral indices with the leading component fading at the highest frequencies, while the trailing component brightens at the highest frequencies. In a subsequent analysis, they report average fluences of 480 and 220 kJy ms for the two bursts, respectively, with a systematic uncertainty of about a factor of 2. The burst detected by STARE2 in the frequency range 1281–1468 MHz is single peaked and the updated fluence is reported as 1.5(3) MJy ms (Bochenek et al. 2020a). These fluences correspond to isotropic equivalent energies of 3×10^{34} erg for an assumed distance of 10 kpc for the CHIME burst (The CHIME/FRB Collaboration et al. 2020) and 2.2×10^{35} erg for an assumed distance of 9.5 kpc for the STARE burst (Bochenek et al. 2020a). This burst is therefore brighter than any radio burst seen from any Galactic source to date and the corresponding energy is between one and two orders of magnitude less than the equivalent energy for the faintest fast radio bursts (FRBs). This has led to the suggestion that this burst can be linked to the low end of an FRB luminosity function thereby associating at least some FRBs with magnetars.

The radio burst detected on 2020 April 28 was temporally coincident with the real-time detection of a bright and hard X-ray burst by the *INTEGRAL* Burst Alert System (Mereghetti et al. 2020), and an X-ray burst from a refined analysis of the *Insight*-HXMT,[1] AGILE (Tavani et al. 2020), and Konus-Wind (Ridnaia et al. 2020) light curves (Zhang et al. 2020a). The *INTEGRAL* X-ray burst light curve in the range 20–200 keV exhibits two peaks separated by $\sim$30 ms, which is consistent with the separation between the two burst components detected by CHIME (Mereghetti et al. 2020; The CHIME/FRB Collaboration et al. 2020). Similarly, *Insight*-HXMT reports likely X-ray and hard X-ray counterparts (27–250 keV) to the double-peaked radio pulse detected by CHIME. Based on the geocentric arrival times of the CHIME and STARE2 pulses, the two-component CHIME burst is well aligned, but not perfectly, with the two peaks in the *INTEGRAL* light curve while the single-peaked STARE2 pulse aligns with the second peak in the *INTEGRAL* light curve. *Insight*-HXMT was also observing (Li et al. 2020) when FAST detected the highly polarized radio pulse. No significant events were found in the X-ray light curves around the time of the radio detection.

The detection of the radio/X-ray burst led to immediate follow-up campaigns with a variety of radio telescopes and some of these radio observations were coordinated with the X-ray observations. In the immediate aftermath, no radio emission or pulses were detected from the source using the Green Bank Telescope (GBT; Surnis et al. 2020a) or the Deep Space Network (DSN) telescope (Pearlman et al. 2020). Apart from the one faint, polarized radio pulse, no other bursts were seen in the subsequent few weeks with FAST (Lin et al. 2020a) despite there being 29 SGR bursts detected with the *Fermi* Gamma-ray Burst Monitor during the time window of FAST observations. At the same time, the source continued to show X-ray bursting activity, albeit with a decreasing frequency and mostly weaker bursts. However, some were at least as bright as the one seen concurrently with the radio burst (Borghese et al. 2020a). Observations with the Westerbork single 25-m dish RT1 (*P* band, 313.49–377.49 MHz), the Onsala 25-m telescope (*L* band, 1360–1488 MHz), and the Torun 32-m telescope (*C* band, 4550–4806 MHz) took place when the source emitted two X-ray bursts with no simultaneous radio detections (Kirsten et al. 2020b). Later in the same campaign, on 2020 May 24, two radio bursts separated by just 1.4 s, which is much

[1] http://en.hxmt.cn/bursts/331.jhtml.

less than the pulse period, were detected at 1.3 GHz with a single antenna of the Westerbork Telescope, with fluences of 112 ± 22 and 24 ± 5 Jy ms, respectively. This was followed by a lack of reported pulsed radio emission for almost four months until 2020 October when the source emitted three radio pulses that were detected by the CHIME telescope (Good & CHIME/FRB Collaboration 2020) and which all arrived within one pulse period. Prompt follow-up by the FAST telescope resulted in the detection of a number of single pulses from the magnetar and were able to independently derive its spin period (Zhu, Wang & Zhou 2020). It is thus apparent that SGR J1935+2154 is able to emit radio pulses over a range of pulse energies spanning nearly seven orders of magnitude and is possibly transitioning into a radio-loud magnetar.

Here, we present the results of a long radio follow-up campaign with a number of radio telescopes in order to characterize any radio emission from SGR J1935+2154 in the period after the detection of the 2020 April bright radio burst. The observations are described in Section 2 and the results of the observing campaign are presented in Section 3. We discuss possible implications of our findings in Section 4 and draw our conclusions in Section 5.

2 OBSERVATIONS

Simultaneous multiwavelength observations across a wide spectral range and regular monitoring for further radio emission, either in bursts or periodic emission, would provide valuable insights and new information on the young magnetar to FRB connection. To this end, a number of observing campaigns were initiated. A multitelescope campaign was undertaken to monitor SGR J1935+2154 on 2020 May 11 and 15. The magnetar was observed by the Effelsberg (4–8 GHz), MeerKAT (900–1700 MHz; tied-array beam and imaging), LOFAR (110–190 MHz), and *NuSTAR* (3–79 keV) telecsopes on 2020 May 11, and the MeerKAT (900–1700 MHz) and *Insight*-HXMT telescopes on 2020 May 15 and with the MeerLICHT optical telescope between 2020 May 10 and 21. Additionally, simultaneous coordinated observations in the radio and X-ray between Arecibo and *Swift*/XRT and NICER were organized on 2020 May 13 and 18. The details of these coordinated observations are summarized in Table 2 and described below. We also undertook a long-term monitoring campaign at the Northern Cross (NC) and MK2 radio telescopes that are summarized in Table A1 and also described below. For each observation, we also checked for radio overlap with any X-ray bursts that were detected by all-sky X-ray burst monitors like *Swift*-Burst Alert Telescope and *Fermi* Gamma-Ray Burst Monitor (Lin et al. 2020b; Tohuvavohu 2020).

2.1 Arecibo

We observed SGR J1935+2154 using the Arecibo radio telescope over two epochs on 2020May 13 and 18. For the first epoch, we used the L-Wide receiver (1.15–1.73 GHz). Channelized data with full Stokes polarisation information were recorded using the PUPPI backend (see Deneva et al. 2013, and the references therein). The data were sampled at 10.24 μs over a usable bandwidth of 600 MHz. We also performed a 90-s calibrator scan before the observations for polarimetric calibration. For the second epoch, we recorded total intensity data with 40.96-μs time resolution over the same usable bandwidth and the same frequency range. The details of the observations are presented in Table 2. The recorded data were then searched offline for bright single pulses from the magnetar. The channels corrupted by strong radio frequency interference (RFI) were masked from further processing. Then, the resulting filterbank data were searched using the HEIMDALL single-pulse detection software,[2] over a DM range of 300–400 pc cm^{-3}, which covers the DMs of the bursts already presented in the literature. All the resultant candidates from the single pulse search above a signal-to-noise (S/N) of 7 were visually inspected for any signs of broad-band astrophysical origin.

2.2 Effelsberg

At the Effelsberg 100-m Telescope, SGR J1935+2154 was observed 14 times from 2020 April 30 at three different frequency bands (see Table 2). Signals from the *L*-, *S*-, and *C*-band receivers were converted into pulsar search mode data at 32-bit resolution. The wide-band CX-receiver signal was mixed down to two 0–2 GHz bands and digitally processed to generate 4096-channel, 8-bit pulsar search mode data with a time resolution of 131.072 μs. The data were subsequently searched for any dispersed pulses and periodic pulsed emission. To detect periodic emission, the data were folded using an ephemeris constructed from Israel et al. (2016) and using a DM of 332.8 pc cm^{-3} (Scholz 2020). After cleaning the data for impulsive RFI, dispersed radio bursts were searched for using the `single_pulse_search.py` utility from the PRESTO[3] (Ransom 2011) software suite, over a DM range of 300–400 pc cm^{-3}. Single pulse candidates with S/N above 7σ were visually inspected.

2.3 LOFAR

We used LOFAR, the Low Frequency Array (Stappers et al. 2011; van Haarlem et al. 2013), to observe SGR J1935+2154 for 6 h, split into 2-h observations starting at 01:49, 04:01, and 06:13 UTC on 2020 May 11. The observation was configured to obtain simultaneous interferometric and beamforming products from the COBALT correlator and beamformer (Broekema et al. 2018), to allow low-time, high-spatial resolution imaging of the field of SGR J1935+2154 as well as high-time resolution, low-spatial resolution beamformed observations of SGR J1935+2154. The beamformed data products used signals from the 23 LOFAR High-Band Antenna (HBA) core stations to form a tied-array beam pointed at SGR J1935+2154. A second tied-array beam was pointed towards the millisecond pulsar and giant-pulse emitter, PSR B1937+21, offset by 1.°3 from SGR J1935+2154 to serve as a test of our analysis pipelines. The results of LOFAR imaging will be presented elsewhere. Our data analysis follows that detailed in Chawla et al. (2020) and Bassa et al. (2020); we will briefly describe it here. Dual-polarization complex voltages were recorded for 47 MHz of bandwidth for frequencies between 120.2 and 167.1 MHz. To allow simultaneous interferometry and beamforming, the bandwidth is somewhat reduced from the observational setup used in Bassa et al. (2020), which obtained only beamforming products. Using `cdmt` (Bassa, Pleunis & Hessels 2017), the complex voltages were coherently dedispersed to a dispersion measure of DM = 332.8 pc cm^{-3} (Scholz & CHIME/FRB Collaboration 2020; Bochenek et al. 2020a) to create dynamic spectra with 163.84-μs and 24.41-kHz time and frequency resolution, respectively. Radio frequency interference was removed with RFIFIND from PRESTO.

To allow for searches over a wide range of pulse widths, as at this DM we might expect significant scattering at LOFAR frequencies, the dynamic spectra were downsampled to 655.36-μs time resolution and 97.65-kHz frequency resolution (using incoherent dedispersion

[2] https://sourceforge.net/projects/heimdall-astro/.
[3] https://github.com/scottransom/presto.

Table 2. Summary of radio and optical observations.

Telescope	T_{start} (UTC)	T_{end} (UTC)	F_{centre} (MHz)	BW (MHz)	N_{chan}	t_{samp} (μs)	RBF (mJy ms)	Flux (μJy)
Arecibo	2020-05-13 09:13:16	2020-05-13 09:56:00	1380	600	4096	10.24	25	4.5
Arecibo	2020-05-18 08:51:09	2020-05-18 09:40:00	1380	600	2048	40.96	25	4.3
Effelsberg	2020-04-30 07:32:40	2020-04-30 08:32:20	1360	240	256	51.2	169.54	29.95
Effelsberg	2020-05-01 00:00:10	2020-05-01 00:59:40	1360	240	256	51.2	169.54	29.87
Effelsberg	2020-05-01 02:39:20	2020-05-01 05:51:30	1360	240	256	51.2	169.54	16.64
Effelsberg	2020-05-06 06:16:10	2020-05-06 07:15:20	1360	240	256	51.2	169.54	29.95
Effelsberg	2020-05-07 05:45:30	2020-05-07 09:47:50	1360	240	256	51.2	169.54	14.94
Effelsberg	2020-05-08 07:02:10	2020-05-08 08:02:10	4850	500	512	51.2	121.94	21.29
Effelsberg	2020-05-11 03:36:54	2020-05-11 08:36:10	6000	4000	4096	131.072	63.63	5.00
Effelsberg	2020-05-19 01:16:20	2020-05-19 02:58:00	2550	80	256	102.4	200.64	27.12
Effelsberg	2020-05-20 04:55:50	2020-05-20 06:55:50	1360	240	512	102.4	169.54	21.08
Effelsberg	2020-05-28 03:31:50	2020-05-28 07:31:50	2550	80	256	102.4	177.34	22.0
Effelsberg	2020-06-04 02:41:30	2020-06-04 04:41:30	1360	240	256	102.4	169.54	21.08
Effelsberg	2020-06-06 23:18:49	2020-06-07 01:18:49	2550	80	256	102.4	177.34	22.05
Effelsberg	2020-06-08 03:03:39	2020-06-08 07:03:49	1360	240	256	102.4	169.54	21.08
Effelsberg	2020-06-22 23:49:40	2020-06-23 04:44:50	1360	240	256	102.4	169.54	12.24
LOFAR	2020-05-11 01:49:00	2020-05-11 03:49:00	144	47	480	655.4		
LOFAR	2020-05-11 04:01:00	2020-05-11 06:01:00	144	47	480	655.4		
LOFAR	2020-05-11 06:13:00	2020-05-11 08:13:00	144	47	480	655.4		
MeerKAT[a]	2020-04-29 02:39:27	2020-04-29 06:58:21	1284	856	1024	38.28	75	
MeerKAT[b]	2020-05-08 05:16:48	2020-05-08 06:33:36	1284	800, 856	1024, 4096	38.28, 306.24	75	
MeerKAT[b]	2020-05-11 03:01:01	2020-05-11 06:18:32	1284	800, 856	1024, 4096	38.28, 306.24	75	
MeerKAT[b]	2020-05-15 00:41:00	2020-05-15 04:00:14	1284	800, 856	1024, 4096	38.28, 306.24	75	

Telescope	T_{start} (UTC)	T_{end} (UTC)	Bands	No. exp.	t_{exp} (s)	Lim. mag. (AB)	Lim. flux (μJy)
MeerLICHT	2020-05-10 02:24	2020-05-10 03:00	*u*, *g*, *q*, *r*, *i*, *z*	3 × 6	60	19.75	45.88
MeerLICHT	2020-05-15 02:49	2020-05-15 03:00	*u*, *g*, *q*, *r*, *i*, *z*	1 × 6	60	20.43	24.35
MeerLICHT	2020-05-15 03:11	2020-05-15 04:26	*q*	34	60	20.41	24.92
MeerLICHT	2020-05-17 02:49	2020-05-17 03:00	*u*, *g*, *q*, *r*, *i*, *z*	1 × 6	60	20.64	20.15
MeerLICHT	2020-05-17 03:14	2020-05-17 04:19	*q*	27	60	20.73	18.60
MeerLICHT	2020-05-18 02:52	2020-05-18 03:02	*u*, *g*, *q*, *i*, *z*	1 × 5	60	20.60	20.82
MeerLICHT	2020-05-18 03:05	2020-05-18 04:20	*q*	32	60	20.79	17.59
MeerLICHT	2020-05-19 02:50	2020-05-19 03:00	*u*, *g*, *q*, *r*, *i*, *z*	1 × 6	60	18.40	159.06
MeerLICHT	2020-05-19 03:02	2020-05-19 04:19	*q*	25	60	20.70	19.14
MeerLICHT	2020-05-21 03:06	2020-05-21 03:19	*u*, *g*, *q*	1 × 3	60	20.16	31.25

Notes. The two Arecibo observations were coordinated with *Swift* and NICER, respectively. The radio burst fluence limits is denoted as RBF assuming a burst width of 1 ms. Both the RBF and the average pulse flux limits (the final column) correspond to a signal-to-noise ratio (S/N) of 7 (S/N 5 for the optical observations). Optical limits correspond to the deepest (*q*) band. See Appendix B for a full overview of the optical observations.
[a]Beam-formed.
[b]imaging and beam-formed.

at DM = 332.8 pc cm^{-3}), and incoherently dedispersed in steps of 0.01 pc cm^{-3} for DMs between 325 and 375 pc cm^{-3} using the `dedisp` algorithm (Barsdell et al. 2012a). Pulses with widths from the native time resolution up to 50 ms were searched for using a GPU-accelerated version of PRESTO's `single_pulse_search.py`. To remain sensitive to pulses with even greater widths, the analysis was repeated on dynamic spectra downsampled to 20.971 ms, with incoherent dedispersion steps of 0.2 pc cm^{-3} and pulse widths up to 3.7 s. Given the nominal 313-μs scattering width of bursts detected at 1324 MHz (Kirsten et al. 2020a), at LOFAR frequencies scattering would dominate, and pulse widths of the order of ∼2 s would be expected.

2.4 MeerKAT tied-array beam

We recorded the beam-formed output of typically 60 MeerKAT antennas with the (PTUSE) backend (Bailes et al. 2020) in both fold and search-mode. The search-mode data have a sampling time of 38.28 μs, 8-bit resolution, and 1024 frequency channels across the 856-MHz bandwidth. The folded data have 8-s integrations, 1024 phase bins across the profile, and 1024 frequency channels. Both data sets are stored in PSRFITS format (Hotan, van Straten & Manchester 2004). We subjected the data to a variety of searches. First, we visually inspected the folded data for pulsed emission after standard RFI excision. Secondly, we created single-pulse archive files from the search-mode data using an ephemeris based on Israel et al. (2016) (as in Section 2.2) and visually inspected those. Moreover, we ran single-pulse tools on them that we developed for data analysis of rotating radio transient pulsars (Jankowski et al., in preparation). Finally, we aggregated the data into 1-min integrations and converted them to SIGPROC[4] filterbank format using tools from the PRESTO syes, oftware suite. We then searched them using the HEIMDALL software for trial DMs between 0 and 600 pc cm^{-3}. We utilized standard RFI excision methods, including a static RFI mask that left us with an effective bandwidth of about 630 MHz. We visually inspected all

[4]https://sigproc.sourceforge.net.

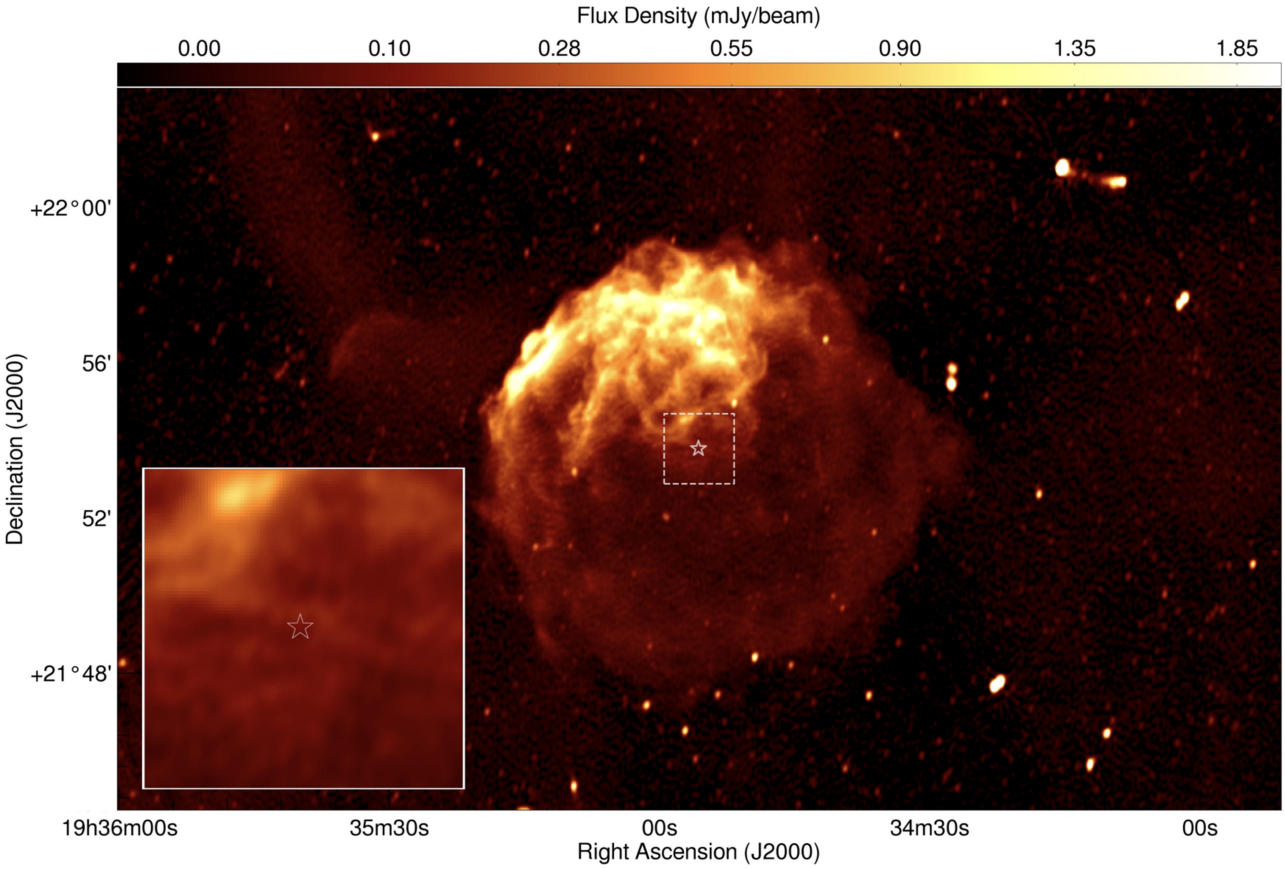

Figure 1. The inner $0.5 \times 0.3\,\mathrm{deg}^2$ of the target field, formed by combining the 2020 May 11 and 15 MeerKAT observations. The position of SGR J1935+2154 is marked with a star, embedded in the emission from SNR G57.2+00.8, which dominates the field. The thermal noise in this image is approximately 5.2 μJy beam^{-1}. The restoring beam in this image is a 2D Gaussian with an extent of $8.4 \times 5.8\,\mathrm{arcsec}^2$ (position angle 178°, east of north). The inset panel shows a $1.8 \times 1.8\,\mathrm{arcmin}^2$ zoom on the location of SGR J1935+2154, as marked by the dashed box on the main panel. The colourmap has a square-root stretch function, and is the same for both panels. Pixel values in mJy beam^{-1} are indicated at the top of the figure.

resulting candidates with S/N above 7, pulse widths up to about 39.2 ms, and DMs between 300 and 360 pc cm^{-3}, i.e. in a window around the nominal DM of the magnetar.

Additionally, during the observations on UTC 2020 May 8, 11, and 15, the MeerTRAP single-pulse pipeline running on the TUSE instrument (Transients User Supplied Equipment; Stappers et al., in preparation) undertook a real-time search for single pulses. Using the innermost 40 MeerKAT dishes, it searched 768 full-bandwidth (see Table 2) beams formed by the FBFUSE backend (Filter-bank Beamformer User Supplied Equipment; Barr et al., in preparation). These dTata had a time resolution of 306.24 µs. The beams were placed so that they overlapped at 25 per cent of the peak sensitivity and covered a total area of 0.8 deg^2 centred on the position of SGR J1935+2154.

2.5 MeerKAT imaging

Imaging-mode observations of SGR J1935+2154 were carried out with MeerKAT on three occasions (see Table 2 for the dates). The data reduction procedure[5] was consistent for each epoch. The visibilities were averaged from their native 4096 channels to 1024 channels. Basic flagging commands were applied to all the data using the CASA package (McMullin et al. 2007), including the flagging of persistent RFI bands on baselines below 600 m. Auto-flagging was performed on the calibrators using the TFCROP and RFLAG algorithms within CASA using their default settings. Delay and bandpass solutions were iteratively obtained from observations of the primary calibrator PKS B1934−638 with rounds of flagging in between iterations. PKS B1934−638 was also used to set the absolute flux scale. Time-dependent gains were derived from observations of J2011−0644, which was observed for 2 min for every 20 min of target observation. The target data were corrected using these calibration solutions, and then flagged using TRICOLOUR[6] (Perkins, Merry & Smirnov 2020).

The target data were imaged using WSCLEAN (Offringa et al. 2014) with multiscale cleaning (Offringa & Smirnov 2017) and iterative masking. Phase-only self-calibration solutions were derived for every 128 s of data, and amplitude and phase corrections were solved for once per 20-min scan using CASA. These solutions were applied and the imaging process was repeated. To fully model and deconvolve off-axis emission, the images consisted of 10 240^2 pixels of 1.1×1.1 arcsec^2. A Briggs' weighting parameter of −0.8 was used to temper the sensitivity to large-scale radio structures. In addition, a Gaussian taper was applied to the (u, v) plane to obtain a 5-arcsec synthe-

[5]MeerKAT calibration and imaging scripts are available here: https://ascl.net/2009.003 (Heywood 2020).

[6]https://github.com/ska-sa/tricolour.

sized beam. No primary beam correction was applied. The inner $0.5 \times 0.3\,\mathrm{deg}^2$ of the resultant image of the field is shown in Fig. 1.

In addition to the three observations made in 'standard' imaging mode, we also obtained visibilities from the beamformer mode observation on 2020 April 29. No calibrator scans were available for this run. The data were simply flagged using TRICOLOUR, and then the multifrequency, multiscale clean component model from the 2020 May 15 run was used to predict model visibilities to self-calibrate the data.

2.6 MK2 observations

We also initiated a monitoring campaign of SGR J1935+2154 using the 32-m Mark 2 (MK2) radio telescope located at Jodrell Bank Observatory. The source was monitored with almost daily cadence at 1532 MHz in separate 1-h observations from 2020 May 30, with a consistent observing setup. For each observation, a 400-MHz band was coarsely channelized into 25 subbands of 16 MHz each with a polyphase filter using a ROACH-based backend (Bassa et al. 2016). For the single pulse search, each 16-MHz subband was further channelized into 32 frequency channels using `digifil` from the `dspsr` software suite (van Straten & Bailes 2011), and downsampled to a sampling time of 256 μs. After removing edge channels and known RFI, the resulting data span approximately 400 MHz, split into 672 frequency channels. We then masked further frequency channels in the data containing narrow-band RFI. The resulting data were then searched for significant signals (S/N > 7) over a small range of DM (325–335 pc cm^{-3}) around the nominal value for the magnetar using `heimdall` (Barsdell et al. 2012b). We also used the digital filterbank (DFB) backend, which incoherently dedispersed and folded the data at the DM and period of the magnetar using the best known ephemeris of SGR J1935+2154 from Israel et al. (2016). After RFI removal, a bandwidth of approximately 336 MHz was used. The operational details of the DFB backend are provided in Manchester et al. (2013).

2.7 Northern Cross

Observations with the NC radio telescope were carried out for approximately 1.5 h during transit for 35 d starting on 2020 April 30 and ending on 2020 June 12. The few interruptions during this period (see Table A1) were due to technical issues or to the use of the antenna for other observations. The system, upgraded to observe FRBs, is described in Locatelli et al. (2020). Only a portion of the north–south arm (6 cylinders out of 64) was used in this observing campaign. The system is composed of 24 radio receivers (4 receivers per cylinder) and it has an effective area of $\simeq$750 m^2. Signals from the 24 receivers were calibrated by observing Cas A in interferometric mode, and then a single digital beam was formed, which followed the source as it transited across the field of view. Beam-formed voltages were stored to disc with a 138.24-μs time resolution. The system operates in the 400–416 MHz frequency band, with 12.2-kHz frequency resolution. The data were searched for bursts as wide as 100 ms using HEIMDALL. Data were also folded in search of pulsations using the spin period measured from the *NuSTAR* X-ray telescope data (Borghese et al. 2020b) and the DM of the FRB-like bursts detected on 2020 April 28 (The CHIME/FRB Collaboration et al. 2020; Bochenek et al. 2020a).

2.8 MeerLICHT

MeerLICHT is the optical wide-field imager that is twinned with the MeerKAT radio array (Bloemen et al. 2016). It features a 65-cm primary mirror and the modified Dall-Kirkham design gives it a field of view of 2.7 deg^2, sampled at 0.56 arcsec pixel^{-1} with an STA 1600 10560 × 10560 CCD. MeerLICHT is equipped with a Sloan-type filter set (*u*, *g*, *r*, *i*, *z*) and additionally has a wide-band (440–720nm) *q*-band filter. Between 2020 May 10 and 21, the field of SGR J1935+2154 was observed a total of 162 times in 60-s integrations, using all six filters. All data was processed automatically by the `BlackBOX` pipeline, developed for the MeerLICHT and BlackGEM projects. `BlackBOX` performs standard optical calibrations (de-biasing, overscan corrections, flat-fielding) as well as astrometric and photometric calibrations. The astrometry is based on the *Gaia* DR2 catalogue, with after-calibration rms values of <50 mas in both coordinates, across the full field. The photometry is calibrated using a set of 70 million all-sky standard stars that have their spectral-energy distribution reconstructed from *Gaia*, SDSS, PanStarrs, SkyMapper, *GALEX*, and 2MASS catalogues. Uncertainties on the photometric zero-point per image are at the level of 1 per cent. Output from `BlackBOX` includes a full-source catalogue of all detected sources, as well as a transient catalogue of transient and/or high-variability sources. The last is based on difference imaging that is performed using the `ZOGY` (Zackay, Ofek & Gal-Yam 2016) algorithms. As the MeerLICHT/BlackGEM sky grid field containing the position of SGR J1935+2154, with FieldID 11744, had not been observed yet as part of the MeerLICHT Southern All-Sky Survey that covers the full sky south of declination +30°, the first image on the field in each filter is taken to be the reference image for the image differencing routines. If a transient source is also present in the reference image, it is only detected as a transient if it changes it flux significantly between the reference image and the subsequent images. However, it would then also be present in the full-source catalogue of objects. `BlackBOX` includes a quality control step, where observations are flagged according to a colour-coding (green, yellow, orange, or red) based on a set of numerical estimates on the quality of the observations. For the data obtained here, all the *u*-band data were red-flagged due to a too high standard deviation of the photometric zero-point over the field of view. This means that all *u*-band data did get processed but no transient detection algorithm was applied. MeerLICHT/BlackGEM magnitudes are on the AB system. Limiting magnitudes are calculated from the detected sources and represent the brightness of a source that would have been detected at the 5σ level. `BlackBOX` calculates both field-level limiting magnitudes, i.e. a single value across the full field, as well as position-dependent limiting magnitudes for transients. For example, the position-dependent limiting magnitude can vary significantly from the field-level limiting magnitude for transients located on top of bright galaxies.

All MeerLICHT observations were analysed on a per-exposure basis. Afterwards, co-adds of all the images taken in the same filter were made, for the possible detection of a fainter counterpart. An image of the field from the deep co-add in the *q* band (440–720nm) surrounding SGR J1935+21 is shown in Fig. 2. An overview of the MeerLICHT data is shown in Table 2. A detailed log of MeerLICHT observations is given in Table B1.

3 RESULTS

3.1 Radio non-detections

No potential candidates were found in any of the single pulse searches of the Arecibo data from both epochs (see Table 2) and we report an upper limit on the fluence of a potential single pulse from the magnetar of 0.09 Jy ms for a 5-ms-wide pulse, under the assumption that the emission spans the available bandwidth. Simultaneous

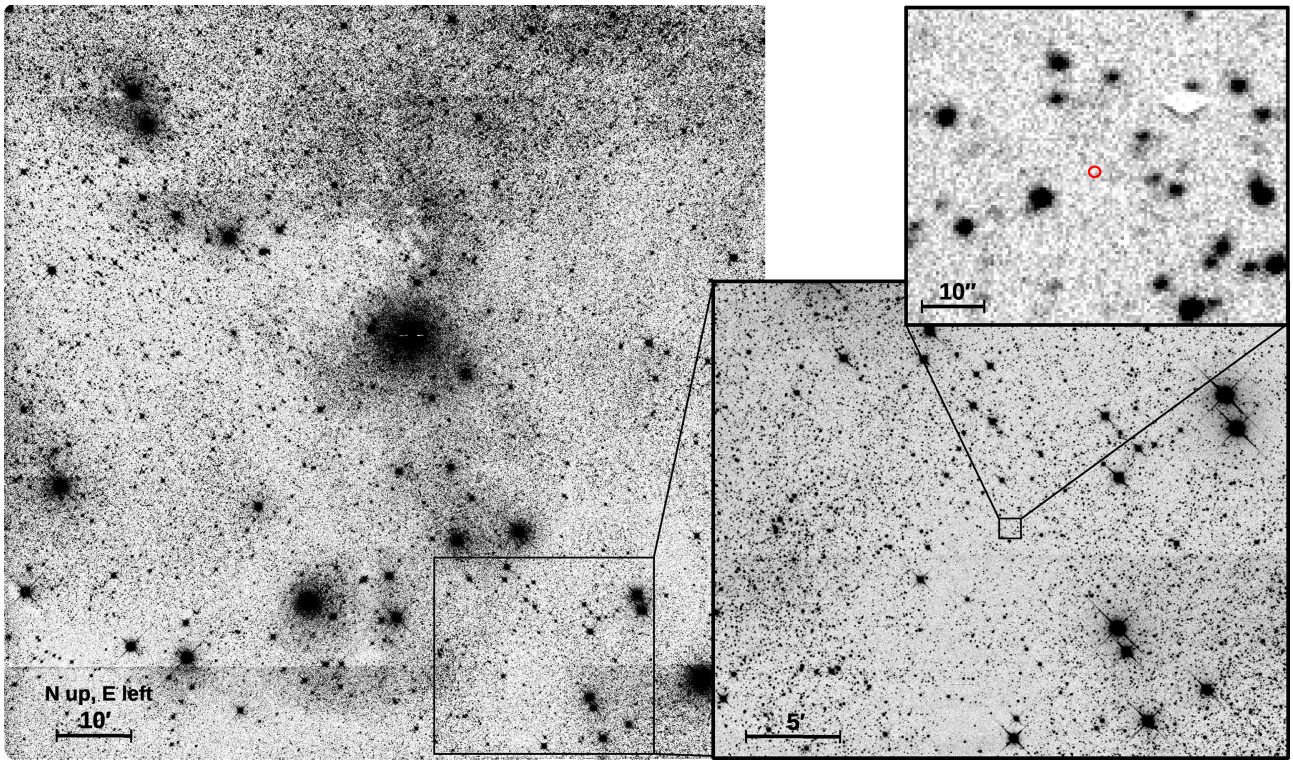

Figure 2. Co-added MeerLICHT q-band image of the field of SGR J1935+2154. Left-hand panels: the full field with ID 11744, spanning $1.65 \times 1.65\,\mathrm{deg}^2$. Darker regions, e.g. at the top panels, are the results of denser star field. Lighter regions show the effect of obscuring dust lanes. The horizontal stripe at the bottom is a low-level artefact of the border between two read-out channels. Bottom right-hand panel: a $30 \times 30\,\mathrm{arcmin}^2$ zoom-in centred on the position of SGR J1935+2154 and matching the size and orientation of the MeerKAT SNR image shown in Fig. 1. Top right-hand panel: a $1 \times 1\,\mathrm{arcmin}^2$ close-up of the region centred on SGR J1935+2154. The red circle indicates the position of SGR J1935+2154. Faintest detected sources are at the level of $\mathrm{AB}_q = 22.8$ mag.

observations took place with the *Swift*/XRT instrument in photon counting mode during the Arecibo time window on 2020 May 11. No coincident bursts were detected (Borghese et al. 2020a). Similarly, simultaneous observations with the *NICER* X-ray telescope on 2020 May 18 did not result in coincident detections either (A. Borghese, private communication). No periodic or transient signals above 7σ were detected in the Effelsberg observations. The sensitivities of the receivers used for these observations vary across the observing band or between the two orthogonal probes of the receiver.[7] The detection limits in Table 2 are based on an average value of 25, 18, 11, and 17 Jy for the system equivalent flux density of the *CX*-, *C*-, *S*-, and *L*-band receivers for an S/N of 7σ and 10 per cent duty cycle. No bursts were found in either analysis method of the LOFAR observations (see Section 2.3). We estimate the sensitivity limits for LOFAR by using the radiometer equation and the method detailed in Kondratiev et al. (2016), which uses the Hamaker (2006) model for the LOFAR HBA beam, combined with system temperature estimates, RFI fraction and beamformer coherence. Based on this, we determine 150-MHz fluence limits of 48 Jy ms for a 20-ms burst at an S/N of 7, 260 Jy ms for a 200-ms burst at an S/N ratio of 12, and 440 Jy ms for a 2-s burst at an S/N of 15. Similarly, no credible pulses were detected in any of our MeerKAT searches, which translates to a peak flux density upper limit of about 75 mJy at a frequency of 1.28 GHz, and corresponds to a fluence upper limit of 75 mJy ms, assuming 1-ms pulse width. No credible detections were made in the MeerKAT/MeerTRAP real-time searches on 2020 May 8, 11, and 15 either (see Section 2.4 for more details). The analysis of the NC data produced a series of candidates that were visually inspected if they exceeded an S/N of 7. This revealed no detections down to a limiting sensitivity of 18 Jy ms for a 1-ms burst. For the observations with the MK2 telescope we use a gain of approximately 0.2 K Jy^{-1}, a receiver temperature of 45 K, taking into account the excess sky temperature due to the SNR and a duty cycle of 3 per cent. We report a 7σ flux density limit of 232.1 μJy for pulsed radio emission. For a 7σ single pulse with a width of 1 ms, we report a peak flux limit of 1.92 Jy. We note that the ephemeris (Israel et al. 2016) used for the searches for average pulse emission was somewhat out of date for a variable source like a magnetar, and so all these searches also searched in a range of periods about that predicted by the ephemeris. This range included periods predicted by the more up to date NICER-based ephemeris (Younes et al. 2020b).

Two X-ray bursts on 2020 May 11 at UTs 02:52:18.000 and 04:22:52.560 with fluences 4.91×10^{-10} and $1.35 \times 10^{-8}\,\mathrm{erg\,cm}^{-2}$, respectively, were detected by *Insight*-HXMT in the MeerKAT observing window (see table 4 for details). The second of the bursts also fell in the Effelsberg observing window. Another X-ray burst was detected by the *Insight*-HXMT on 2020 May 15 at 00:37:16.000 with a fluence of $8.64 \times 10^{-12}\,\mathrm{erg\,cm}^{-2}$, which also occurred during the MeerKAT observations. As described above, no pulses were detected at Effelsberg nor at MeerKAT. In Fig. 3, we show a timeline of the single-pulse fluence upper limits at various radio frequencies from this work, together with a selection of measurements reported in the literature. We additionally mark the brightest X-ray bursts detected by *Insight*-HXMT.

[7] https://eff100mwiki.mpifr-bonn.mpg.de/doku.php?id=information_for_astronomers:rx_list.

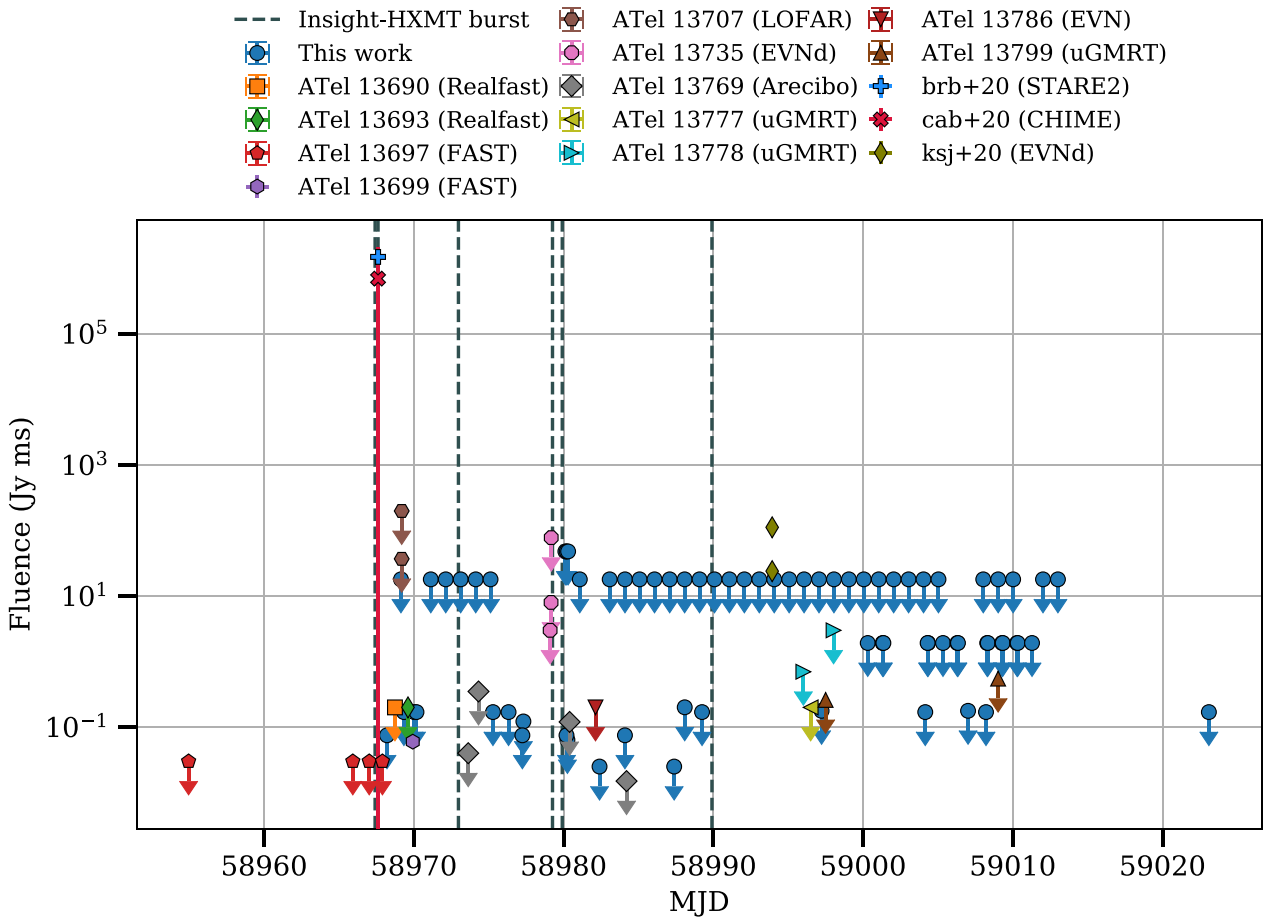

Figure 3. Timeline of the single-pulse fluence upper limits of SGR J1935+2145 at various radio frequencies as presented in this work, together with a selection of measurements from the literature. Fluences from this work are quoted for assumed burst widths of 1 ms (see Tables 2 and A1), except in the case of the low-frequency LOFAR observations, where pulse scatter-broadening effects likely dominate. Additionally, we mark the times of the brightest X-ray bursts with fluences $>10^{-7}$ erg cm^{-2} reported by *Insight*-HXMT.

Fig. 1 shows the MeerKAT radio image made from the imaging data obtained during the simultaneous beam-formed observations. The radio image shows the SNR G57.2+00.8 as a complete circular shell with a brightened north-eastern edge. The enhanced brightness probably indicates that the expanding shock front has encountered dense, molecular interstellar clouds. The high resolution of the image (8.4×5.8 arcsec^2) reveals detailed structure of the bright filaments. The low-surface-brightness emission towards the south-western end of the SNR shell shows the two arc-like features also seen by Kothes et al. (2018) in the 150-MHz GMRT map. In a region 33×33 arcsec^2 centred on the known magnetar position we measure a root mean square flux of 29, 25, and 22 μJy beam^{-1} for the three imaging epochs (see Table 2), respectively. There is clear presence of diffuse emission associated with the SNR located at the position of the magnetar and the corresponding flux values for the pixel located at the source position are 176, 109, and 103 μJy beam^{-1} for the three epochs, respectively.

3.2 Possible radio detection

A search spanning ±1 ms around the nominal period and ±200 pc cm^{-3} around the nominal DM was carried out on the folded NC data. Observations on 2020 May 30, starting at 00:31:03 UTC and finishing at 02:01:01 UTC, resulted in a marginal detection of a periodic signal with period $P = 3.247\,60(3)$ s, DM = 316(18) pc cm^{-3}. The pulse width was of the order of 100 ms (Fig. 4). Given the system equivalent flux density of the NC, 640 Jy, this 7σ detection implies a flux density of ∼3 mJy. No detections were obtained in any of the other observations, including those performed in the days before and after 2020 May 30, with flux density upper limits for an S/N 6 signal between 2.5 and 5 mJy, depending on the duration of the observation. However, comparison with the period predicted for this epoch using the ephemeris derived from the NICER observations (Younes et al. 2020a) indicates a difference in period of approximately 0.2 ms. As can be seen in the top panel of Fig. 4, this offset period lies in the range searched but is clearly not favoured. This therefore suggests that the radio pulse is in fact an unassociated noise fluctuation. During the 35-d NC campaign from 2020 April 30 to June 12, the HXMT reported six bursts at UTs of 02:49:27 on 2020 May 2, 01:50:23 and 02:09:32 on 2020 May 16, 01:54:21 on 2020 May 18, 01:24:06 on 2020 May 21, and 00:57:45 on 2020 May 25. No simultaneous radio bursts were detected.

3.3 Optical MeerLICHT results

No persistent or transient source is detected in the MeerLICHT imaging in any of the exposures and/or filter bands. Per image 5σ source detection limits are given in Appendix B and vary within

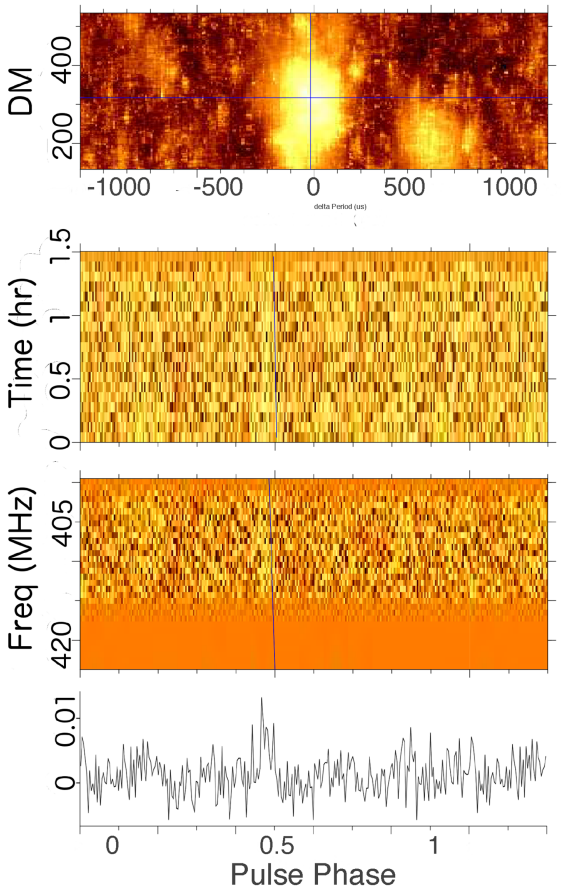

Figure 4. A radio pulse detected during observations of SGR J1935+2154 with the NC (obtained on 2020 May 30). From the bottom to top, the plots show the best integrated pulse profile (vertical axis is in arbitrary units); a waterfall plot of the frequency subbands versus pulse phase (the lighter the colour, the stronger the signal); a waterfall plot of time subintegrations (5 min each) versus pulse phase; and a colour scale showing the S/N of the integrated pulse profile in function of the spin period and dispersion measure (brighter colors correspond to higher values). The values of P and DM maximizing the S/N and corresponding to the bottom profiles are reported in the text. The optimized value of P is inconsistent with that derived from an ephemeris generated from NICER data.

$m_{AB}(u) = 18.5$–19.2, $m_{AB}(g) = 19.3$–20.4, $m_{AB}(q) = 17.8$–20.6, $m_{AB}(r) = 18.9$–19.8, $m_{AB}(i) = 18.8$–19.5, and $m_{AB}(z) = 17.9$–18.2. The depth of each image is a combination of image quality (seeing), throughput through the system and background flux (moon in particular). The image quality in the image was at the level of 3 arcsec, which is a combination of site seeing, tracking residuals and a dome seeing due to a suboptimal airflow through the dome. All non-red-flagged data per filter were co-added for deeper detections. Due to the larger number of observations and the intrinsic sensitivity of the system in the q band, this co-add goes substantially deeper than the other bands. No source is detected at the position of SGR J1935+2154, averaged over the period 2020 May 10–19 down to $m_{AB}(q) = 22.8$. Fig. 2 shows the full field, and a close-up of the area around the source. The area around SGR J1935+2154 shows clear evidence for dust extinction, evidenced by the lower number of star counts over the field. SGR J1935+2154 is located at the edge of one of these dust lanes and it is therefore likely that the sightline to SGR J1935+2154 suffers from appreciable extinction. The association of higher star counts with the direct environment of the brighter stars in this region (the brightest of which is HD 184961) shows the correlation of these brighter stars with the dust clouds, i.e. in the direct area of the stars local 'holes' are blown in the dust clouds, allowing a clearer line of sight to the dense background star field. *Gaia* DR2 parallaxes to the brighter stars shown in Fig. 2, having magnitudes $G = 6.3$–7.5, imply that the dust clouds are located at only 200–300 pc distance and therefore provide a local absorption screen (see Section 4). In the optical, there is no sign of the SNR that shows up prominently in the MeerKAT observations (Fig. 2).

4 DISCUSSION

Since the discovery of the radio burst, there have been extensive follow-up observations of SGR J1935+2154 across the electromagnetic spectrum. The lack of another radio pulse coincident with an X-ray flare puts interesting constraints on the emission mechanism and begs the question of whether we should be able to see such radio bursts in other active Galactic magnetars. In this context, connecting FRBs with extragalactic magnetars is tantalizing. Current theories that propose FRB emission from a magnetar can be broadly divided into two categories: (1) far-away models, where the FRB is generated by a maser away from the neutron star, and (2) close-in models where the FRB is produced in the magnetospehere of the star. The maser emission model runs into difficulties when explaining all the observed radio and X-ray properties of the contemporaneous radio/X-ray burst seen from SGR J1935+2154 (see Lu, Kumar & Zhang 2020, for more details). Younes et al. (2020a) have shown that the X-ray burst contemporaneous with the radio burst was spectrally unique compared to all other burst in the activity period and it also supports it having a polar cap origin. Hence, if we assume that FRBs produced by magnetars are created in the magnetosphere close to the polar cap, we can expect them to be significantly beamed (Lu, Kumar & Zhang 2020). This of course also means that the source must still be exhibiting bursts infrequently in the radio and that more of them might be associated with an X-ray burst than we observe. Observational evidence so far does suggest a connection between the X-ray and the radio emission mechanisms prevalent in neutron stars and any changes in one of them affects the other (Archibald et al. 2017). It is believed that while the X-ray bursts and radio pulsations in these sources come from different regions in the magnetosphere, the pair plasma causing the X-ray flares can affect the acceleration of radio-emitting particles. This was shown in PSR J1119−6127, a high B-field radio pulsar where a series of X-ray bursts from the source quenched the radio pulsations with the radio emission returning a few minutes after the last X-ray burst (Archibald et al. 2017).

Rea et al. (2012) have shown that the radio/X-ray relationship in magnetars and high B-field pulsars can be quantified by three fundamental quantities: (1) the quiescent X-ray luminosity; (2) the spin-down luminosity; and (3) the electric potential. The electric potential that is generated above the polar cap of the neutron star is believed to be responsible for creating the charged plasma responsible for pulsed radio emission (Ruderman & Sutherland 1975). Assuming a dipolar spin-down for a neutron star (which may not be correct for a magnetar), the electric potential,

$$V \simeq 4.2 \times 10^{20} \sqrt{\frac{P}{\dot{P}^3}} \text{ statvolts}, \quad (1)$$

where P is the period and $\dot{P}$ is the period derivative. In the left-hand panel of Fig. 5, we show SGR J1935+2154 on the so-called Fundamental Plane of magnetars (Rea et al. 2012); we see an interesting trend. As observed by Rea et al. (2012), magnetars that exhibit radio pulsations tend to show a lower X-ray conversion efficiency; the ratio

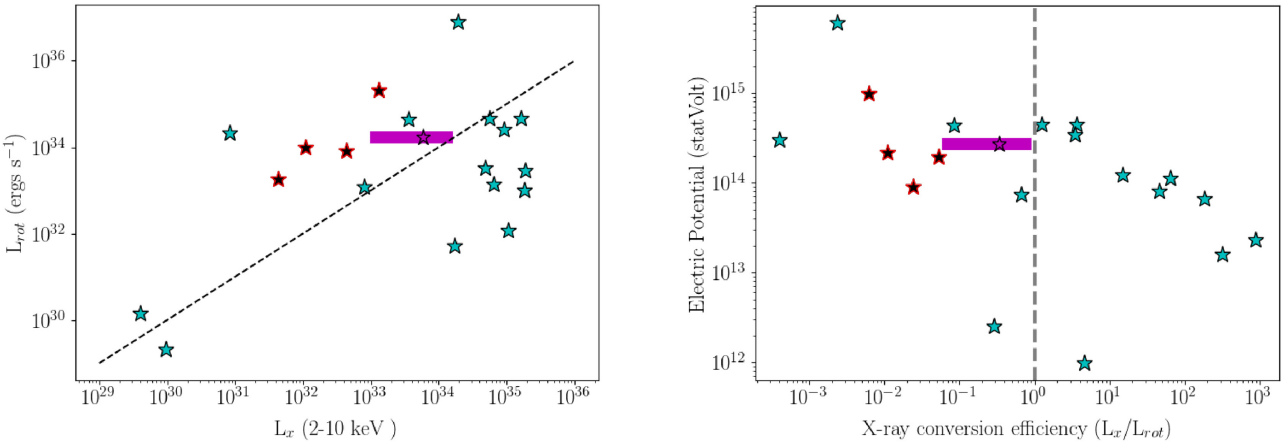

Figure 5. Left-hand panel: spin-down luminosity versus quiescent 2–10 keV X-ray luminosity of magnetars. The black dashed line represents the region where $L_x = L_{rot}$. Right-hand panel: electric potential in the magnetosphere as a function of X-ray conversion efficiency. The grey dashed line corresponds to an efficiency of 1. For both plots, cyan stars represent the magnetar population taken from the McGill Magnetar Catalogue (Olausen & Kaspi 2014). The black stars with red outlines represent radio loud magnetars, while SGR J1935+2154 is shown as the magenta star. The shaded region represents the range of values L_x and conversion efficiency based on the distance to the magnetar (see the text for more details). The position of the magenta star corresponds to the distance of 6.6 kpc as used in Borghese et al. (2020a).

of the quiescent X-ray and spin-down luminosity. The right-hand panel of Fig. 5 suggests that if the X-ray luminosity of the magnetar is larger than the spin-down luminosity, the electric potential generated in the polar cap reduces. This means that the ability to produce coherent radio pulses might be inversely proportional to the ability of the magnetar to produce X-ray emission (see Rea et al. 2012, for more details). If we assume that the marginal detection from the NC telescope of pulsed radio emission from SGR J1935+2154 is genuine, we can associate the ability of the magnetar to produce pulsed radio emission from the magnetic poles to the X-ray efficiency of the source during an active phase. The more efficient a magnetar is in converting the spin-down luminosity and the magnetic energy into X-ray luminosity, the less efficient it is in producing pulsed radio emission. Based on this assumption, SGR J1935+2154 lies very close to the transition from efficient to superefficient regime ($L_x > L_{rot}$) and might explain the intermittent nature of the pulsed emission seen from the magnetar so far. However, we note that the bright radio burst seen on April 28 (Bochenek et al. 2020b; Scholz 2020) and the subsequent detections of single radio pulses apparently emitted within a pulse period over a range of rotational phases (Good & CHIME/FRB Collaboration 2020; Kirsten et al. 2020a) are not consistent with this proposition. One can still argue that the bright single pulses are coming from a different region of the magnetosphere compared to the typical coherent radio emission that we see from radio pulsars. It may also be the case that the radio emission associated with the bright burst is generated by a different physical mechanism or location within the magnetosphere to those seen subsequently with FAST, WSRT, and CHIME. This is also consistent with the fact that the X-ray burst that was contemporaneous with the bright radio burst was unlike the typical X-ray bursts seen from the magnetar and constitutes only ~ 6 per cent of the X-ray bursts seen from SGR J1935+2154 (Ridnaia et al. 2020; Li et al. 2021; Younes et al. 2020a). This emphasizes the need to monitor Galactic magnetars in their active states as they might reveal a peculiar relationship between their radio and X-ray emission properties that will provide more insight into the emission process.

Radio searches for single pulses and average pulse emission by folding the data based on the ephemeris derived from the X-ray observations (e.g. Israel et al. 2016) were carried out using the NC, GMRT (Surnis et al. 2016), and Arecibo (Younes et al. 2017b), on time-scales of days to a few weeks after the outbursts in 2014–2016. Neither telescope reported a detection, and the GMRT quotes upper limits of 0.4 and 0.2 mJy at 326.5 and 610 MHz, respectively, assuming a 10 per cent duty cycle and an 8σ detection threshold. The Arecibo observations were at 6.7 and 1.4 GHz and they report upper limits of 14 and 7 μJy, respectively, having used a 10σ threshold and a 20 per cent duty cycle. However, regular monitoring is supported by the most recent detection of just three pulses with CHIME (Good & CHIME/FRB Collaboration 2020) and the subsequent detection of single pulses and average pulse emission with FAST (Zhu, Wang & Zhou 2020), which also appears to have been transient in nature. It is also unclear how long it takes before the radio emission turns on in these systems. Sometimes it is relatively rapid (e.g. Levin et al. 2019) and other times it can be quite some time after the X-ray outbursts (see Kaspi & Beloborodov 2017, for more details) and can apparently also vary for a given source too. Usually, when a magnetar turns on in the radio, it emits radio pulses during most rotations and stays on, with some significant variability in flux density and pulse shape, over a time-scale of months to years. In the case of SGR J1935+2154, the Kirsten et al. (2020a) campaign lasted for 2 months with a total observing time of 522 h, while our campaign lasted for 1.5 months for a total integration time of $\sim$110 h. Between these two overlapping campaigns, only two radio pulses were seen by Kirsten et al. (2020a). These results along with the the very recent detection of bright radio single pulses and pulsed radio emission from the magnetar (Good & CHIME/FRB Collaboration 2020; Zhu et al. 2020) suggest that the change in the magnetosphere configuration in SGR J1935+2154 to enable pulsed radio emission might be more gradual or sporadic than other magnetars like XTE J1810–197 and Swift J1818.0–1607 where bright radio pulses were seen in the immediate aftermath of the X-ray bursting behaviour. A possible change in the magnetosphere is also supported by X-ray pulsar variations (Younes et al. 2020b). This diversity of emission characteristics emphasizes the need to regularly monitor magnetars in their active states.

The MeerKAT images show no evidence of a point source at the location of SGR J1935+2154 during any of the four observing

epochs (including those taken during the observations on the 29, which also resulted in a non-detection). As mentioned above we quote flux limits only for the first three observing sessions as there was no calibrator scan available for the initial observation that was taken during an ongoing pulsar timing observation. The flux limits are dominated by the presence of the diffuse emission from the SNR. However, they are comparable to those obtained in observations made at similar frequencies with the uGMRT (see table 4), although somewhat worse as the uGMRT resolves out more of the emission. This is why the limit from the European VLBI Network telescopes is also a factor of a few fainter. There was no detection of any persistent or transient optical emission seen with MeerLICHT. The limits from MeerLICHT are in line with the faint infrared counterpart (*F140W*(AB) = 25.3) reported by Levan, Kouveliotou & Fruchter (2018), given the extinction along the line of sight and any reasonable slope on the source's spectrum between the optical and the nIR.

The distance and, perhaps also, the association of SGR J1935+2154 with the SNR G57.2+00.8 is still debatable. This was most recently noted in the paper by Zhong et al. (2020), who pointed out that the distance estimates can be divided into two classes, those that are based on the SNR itself and those that are based on the magnetar. Radio-based studies looking either at the remnant itself or H I and $N_{\rm H}$ and dispersion measure models[8] give distances in the range of 4.5–14 kpc (Pavlović et al. 2013; Surnis et al. 2016; Kothes et al. 2018; Ranasinghe, Leahy & Tian 2018) while a recent study of CO and molecular clouds in the vicinity of the remnant gives a distance of 6.6 ± 0.7 kpc (Zhou et al. 2020). Based on a blackbody spectral fit to the emission of an X-ray flare in a previous outburst, Kozlova et al. (2016) derive a distance upper limit of 10 kpc, while Mereghetti et al. (2020) use their detection of an expanding dust scattering halo during the most recent outburst to constrain the distance to a range 2.2–7.1 kpc. In their paper, Zhong et al. (2020) determine a distance of 9.0 ± 2.5 kpc based mainly on the YMW16 (Yao, Manchester & Wang 2017) dispersion measure based distance model.

With these wide range of distances we note that, although not very accurate, it is possible to put constraints on the distance to SGR J1935+2154 from its detected DM and a relation that links DM to distance within the Milky Way Galaxy. This relation ties together a number of steps, starting with a 3D extinction map within the Galactic plane. From a colour excess–distance relation ($E(g-r)$ versus d), an absorption ($A_{\rm V}$) and colour excess relation, an absorption–hydrogen column density ($N_{\rm H}$) relation, and a hydrogen column density–dispersion measure relation, it is possible to link dispersion measure to distance. The first step is to use 3D dust mapping as in Green et al. (2019), Sale et al. (2009), and Sale et al. (2014). Here we use the results from Green et al. (2019) to link the detected colour excess ($E(g-r)$) to distance. Using Green et al.'s online webtool, the derived relation at the position of SGR J1935+2154 is shown in Fig. 6. The colour-excess in this direction is due to a number of discrete absorption screens, located at a distance (d) of roughly d = 500 pc, 1.5 kpc, and 6.5 kpc. The bright stars and dust clouds shown in Fig. 2 are clearly part of the first of these absorption screens. Th e colour-excess is converted into absorption magnitudes in the Johnson V band, $A_{\rm V}$, using equation (30) from Green et al. (2019):

$$A_{\rm V} = (E(g-r) - C_1)/C_2, \tag{2}$$

where $C_1 = 0.03$ and $C_2 = 0.269$. The conversion from absorption $A_{\rm V}$ to hydrogen column density ($N_{\rm H}$) is derived from X-ray studies

[8]before the magnetar was detected as a radio source.

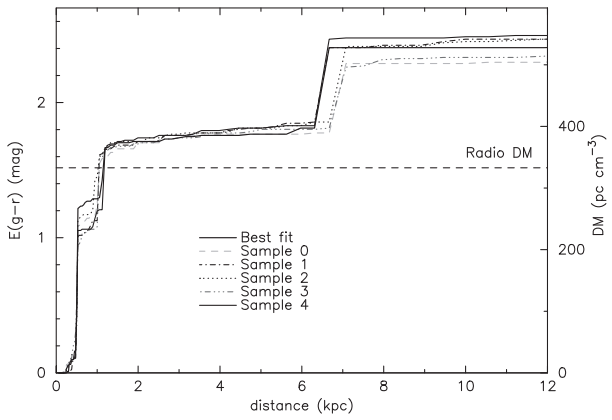

Figure 6. Colour-excess $E(g-r)$ (left-hand axis) and dispersion measure (DM, right-hand axis) as a function of distance, derived from optical data, for the position of SGR J1935+2154, as extracted from the data of Green et al. (2019). Thin lines show the various sample data sets and the thick lines the best fit from Green et al. (2019). To calculate the dispersion measure, equation (5) has been used.

on scattering haloes or X-ray spectral fitting to SNRs and takes the form

$$N_{\rm H} = C_3 A_{\rm V}, \tag{3}$$

where the exact value of C_3 differs between studies (e.g. Gorenstein 1975; Predehl & Schmitt 1995; Güver & Özel 2009; Tian, Su & Xiang 2013). The relation between hydrogen column density and dispersion measure is given by He, Ng & Kaspi (2013) as

$$\mathrm{DM} = N_{\rm H}/C_4, \tag{4}$$

where $C_4 = 0.030^{+0.013}_{-0.009}$, when $N_{\rm H}$ is expressed in units of 10^{21} cm^{-2}. Combining equations (2)–(4) leads to the relation

$$\mathrm{DM} = \frac{C_3(E(g-r) - C_1)}{C_2 C_4}. \tag{5}$$

The final step of relating dispersion measure to distance results from the empirical relation shown in Fig. 6. Using the Predehl & Schmitt (1995) value of $C_3 = 1.79 \pm 0.03$ and evaluating the other constants at their nominal values shows that the colour-excess plateau in Fig. 6 at $1.65 < E(g-r) < 1.83$, corresponding to a distance between 1.2 kpc $< d <$ 6 kpc, leads to a dispersion measure range $360 <$ DM $<$ 400 pc cm^{-3}. The further plateau in extinction at levels of $E(g-r) \geq 2.4$ leads to DM $\geq$ 500 pc cm^{-3} (see Fig. 6). These results are consistent with the results presented by Sale et al. (2014) based on the IPHAS survey (Drew et al. 2005) covering the same coordinates, where the relation is given between distance and monochromatic absorption A_0 evaluated at a wavelength of 5459 Å, corresponding to the central wavelength of the Johnson V band. Given the uncertainties and the fact that $N_{\rm H}$ values determined for magnetars close to the Galactic plane tend to be higher due to X-ray absorption by molecular species rather than just atomic species (He et al. 2013), the value of $N_{\rm H} = 1.1 \times 10^{22}$ cm^{-2} derived from the reddening is consistent with the values determined from spectral fitting by Israel et al. (2016) of $2 \pm 0.4 \times 10^{22}$ cm^{-2}.

Translating the measured DM≈333 pc cm^{-3} directly to distance using this method places the source inside the second absorption screen at a close distance of $d \sim$1.2 kpc. Given the large uncertainties associated with the constants in equation (5), an association on the colour excess plateau within $1.2 < d < 6.5$ kpc is perhaps more likely. Any dispersion measure contribution originating locally to the

source would lower the amount of dispersion measure attributable to the interstellar medium and would potentially favour the closer distance. However, we note that Zhong et al. (2020) suggest that the contribution from the remnant should be small. The upper limit of the reddening derived distance range, about 6.5 kpc is most consistent with other distance estimates based on the magnetar itself, in particular that from the dust scattering halo (2.2–7.1 kpc; Mereghetti et al. 2020) and also with the distance of the SNR determined from the molecular clouds (6.6 ± 0.7 kpc; Zhou et al. 2020). However, 6.5 kpc is at the lower limit of the other distances derived based on methods that use properties or the line of sight to the SNR. The DM of the detected radio pulses does provide a constraint on the distance using models of the dispersion measure but the uncertainty in the DM-derived distance is always fairly large (see Zhong et al. 2020, for a discussion on the distances) especially given that the optical observations suggest that there may significant material at just a few hundred parsecs.

The significant step up in DM suggested from the reddening as shown in Fig. 6 combined with the other measurements means that we favour a distance of around 6.5 kpc for the magnetar. This distance does have some tension with the preferred distances to the SNR but they are not completely inconsistent and therefore do not necessarily imply that the association between SGR J1935+2154 and SNR G57.2+00.8 is in doubt. However, they do argue for a future more detailed study of the association. A distance of 6.5 kpc is nearer than the mean value of around 9 – 10 kpc, which has been used in many papers (e.g. Pavlović et al. 2013; Kozlova et al. 2016; Ranasinghe, Leahy & Tian 2018; Mereghetti et al. 2020; Zhong et al. 2020; Zhou et al. 2020) for determining the luminosity of the initial bright burst detected on 2020 April 28. In their estimates of the energy/luminosity of the April 28 burst CHIME, The CHIME/FRB Collaboration et al. (2020) and STARE2 used distances of 10 and 9.5 kpc, respectively. If we use our nearer distance of 6.5 kpc, this would decrease the energy of the burst by about a factor of 2 and therefore suggest that it is closer to two orders of magnitude fainter than the faintest extragalactic FRBs seen so far. It does however still make it at least a couple of orders of magnitude brighter than anything seen in the Galaxy from a neutron star.

5 CONCLUSIONS

We have presented results from a radio and optical monitoring campaign of SGR J1935+2154 during its active state when it emitted a bright radio burst contemporaneous with an X-ray flare. We observed the source during a number of campaigns that included several simultaneous multifrequency campaigns coincident with X-ray observations as well as longer term monitoring campaigns with a range of telescopes at different frequencies. We failed to detect any single pulses of radio emission despite having observations near in time to the detections made by the EVN project (Kirsten et al. 2020a). A tentative detection of average pulse emission with the NC that was quite close in time to non-detections of average pulse emission and single pulses with other telescopes was ruled out due to the difference in period compared to that derived from X-ray observations. The range of pulse energies at which single pulse emission has been detected, and for apparently brief times, suggests that the source is exceptionally variable, even given the highly variable nature of radio emission seen from the other Galactic magnetars. The location of SGR J1935+2154 in the fundamental radio–X-ray plane for magnetars suggests that the object is on the threshold of how efficiently it can produce radio emission and this might be related to the variety of emission that we see in the radio. Some of the radio observations were coincident with X-ray bursts and so it confirms the model that not all X-ray bursts have associated radio emission, potentially due to geometry, but also the fact that the X-ray burst associated with the April 28 event was significantly different.

We find that there is no persistent or transient radio emission at the X-ray position of the magnetar in the MeerKAT radio images above a best limit of 103 μJy beam^{-1}, indicating that there is no magnetar wind nebula formed that is radio emitting at our detection threshold. There is also no optical emission detected during the period of observation. The optical observations of the field combined with the DM of the magnetar allowed us to obtain a distance estimate for the magnetar that supports a closer distance. This would suggest that the FRB-like burst might be a factor of 2 or more less luminous than previously thought and thus about two orders of magnitude fainter than the least luminous of the known extragalactic FRB pulses. It also suggests that a more detailed study of the association with SNR G57.2+00.8 is needed. This is important as the magnetar models for extra-galactic FRBs is based on them being associated with young magnetars and so one might expect that there would be an associated SNR. The only occasional detections of radio pulses highlighted by our, and other, observing campaigns demonstrates the need of regular multiwavelength follow-up of active magnetars as this may lead us to a better understanding the origins of FRBs.

ACKNOWLEDGEMENTS

The authors would like to thank SARAO for the approval of the MeerKAT DDT request and the CAM/CBF/SP and operator teams for their time and effort invested in the observations. The MeerKAT telescope is operated by the South African Radio Astronomy Observatory (SARAO), which is a facility of the National Research Foundation, an agency of the Department of Science and Innovation. This project has received funding from the European Research Council (ERC) under the European Union's Horizon 2020 research and innovation programme (grant agreement No. 694745). We acknowledge support of the Gravitational Wave Data Centre funded by the Department of Education via Astronomy Australia Ltd and the Australian Research Council Centre of Excellence for Gravitational Wave Discovery (OzGrav), through project number CE170100004. Part of this work has been funded using resources from the research grant *iPeska* (PI: Andrea Possenti) funded under the INAF national call Prin-SKA/CTA approved with the Presidential Decree 70/2016. AP and MBu acknowledge the support from the Ministero degli Affari Esteri e della Cooperazione Internazionale – Direzione Generale per la Promozione del Sistema Paese – Progetto di Grande Rilevanza ZA18GR02.

The MeerLICHT consortium is a partnership between Radboud University, the University of Cape Town, the Netherlands Organisation for Scientific Research (NWO), the South African Astronomical Observatory (SAAO), the University of Oxford, the University of Manchester and the University of Amsterdam, in association with, and partly supported by, the South African Radio Astronomy Observatory (SARAO), the European Research Council, and the Netherlands Research School for Astronomy (NOVA). We acknowledge the use of the Inter-University Institute for Data Intensive Astronomy (IDIA) data intensive research cloud for data processing. IDIA is a South African university partnership involving the University of Cape Town, the University of Pretoria, and the University of the Western Cape. This paper is based (in part) on data obtained with the International LOFAR Telescope (ILT) under project code DDT13_006. LOFAR is the Low Frequency

Array designed and constructed by ASTRON. It has observing, data processing, and data storage facilities in several countries, which are owned by various parties (each with their own funding sources), and that are collectively operated by the ILT foundation under a joint scientific policy. The ILT resources have benefited from the following recent major funding sources: CNRS-INSU, Observatoire de Paris, and Université d'Orléans, France; BMBF, MIWF-NRW, MPG, Germany; Science Foundation Ireland (SFI), Department of Business, Enterprise and Innovation (DBEI), Ireland; NWO, The Netherlands; and the Science and Technology Facilities Council, UK. The Arecibo Observatory is operated by the University of Central Florida, Ana G. Mendez-Universidad Metropolitana, and Yang Enterprises under a cooperative agreement with the National Science Foundation (NSF: AST-1744119). GD, KL, MK, and RK are supported by the European Research Council Synergy Grant BlackHoleCam under contract no. 610058. This publication is based on observations with the 100-m telescope of the Max-Planck-Institut für Radioastronomie at Effelsberg. We would like to thank the referee for the careful reading of this paper.

6 DATA AVAILABILITY

The data underlying this paper will be shared on reasonable request to the corresponding author.

REFERENCES

An T., Hong X., Lao B., Mohan P., Sun X., Wang S., Xu Z., Zhang Z., 2020, Astron. Telegram, 13816, 1
Archibald R. F. et al., 2017, ApJ, 849, L20
Bailes M. et al., 2020, Publ. Astron. Soc. Pac., 37, e028
Barsdell B. R., Bailes M., Barnes D. G., Fluke C. J., 2012a, MNRAS, 422, 379
Barsdell B. R., Bailes M., Barnes D. G., Fluke C. J., 2012b, MNRAS, 422, 379
Bassa C. G. et al., 2016, MNRAS, 456, 2196
Bassa C. et al., 2020, Astron. Telegram, 13707, 1
Bassa C. G., Pleunis Z., Hessels J. W. T., 2017, Astron. Comput., 18, 40
Bera A., Mondal S., Chandra P., Tendulkar S., Roy J., 2020, Astron. Telegram, 13773, 1
Bloemen S. et al., 2016, in Hall H. J., Gilmozzi R., Marshall H. K., eds, Proc. SPIE Conf. Ser. Vol. 9906, Ground-based and Airborne Telescopes VI. SPIE, Bellingham, p. 990664
Bochenek C. D., Ravi V., Belov K. V., Hallinan G., Kocz J., Kulkarni S. R., McKenna D. L., 2020a, Nature, 587, 59
Bochenek C., Kulkarni S., Ravi V., McKenna D., Hallinan G., Belov K., 2020b, Astron. Telegram, 13684, 1
Borghese A., Coti Zelati F., Rea N., Esposito P., Israel G. L., Mereghetti S., Tiengo A., 2020a, ApJ, 902, L2
Borghese A., Rea N., Coti Zelati F., Israel G. L., Esposito P., et al., 2020b, Astron. Telegram, 13720, 1
Broekema P. C., Mol J. J. D., Nijboer R., van Amesfoort A. S., Brentjens M. A., Marcel Loose G., Klijn W. F. A., Romein J. W., 2018, Astronomy and Computing, 23, 180
Burgay M., Israel G. L., Rea N., Possenti A., Zelati F. C., Esposito P., Mereghetti S., Tiengo A., 2014, Astron. Telegram, 6371, 1
Chawla P. et al., 2020, ApJ, 896, L13
Cummings J. R., 2014, GRB Coord. Netw., 16530, 1
Deneva J. S., Stovall K., McLaughlin M. A., Bates S. D., Freire P. C. C., Martinez J. G., Jenet F., Bagchi M., 2013, ApJ, 775, 51
Drew J. E. et al., 2005, MNRAS, 362, 753
Fong W., Berger E., 2014, GRB Coord. Netw., 16542, 1
Gaensler B. M., 2014, GRB Coord. Netw., 16533, 1
Good D., CHIME/FRB Collaboration, 2020, Astron. Telegram, 14074, 1
Gorenstein P., 1975, ApJ, 198, 95
Green G. M., Schlafly E., Zucker C., Speagle J. S., Finkbeiner D., 2019, ApJ, 887, 93
Güver T., Özel F., 2009, MNRAS, 400, 2050
Hamaker J. P., 2006, A&A, 456, 395
He C., Ng C. Y., Kaspi V. M., 2013, ApJ, 768, 64
Heywood I., 2020, Astrophysics Source Code Library, record ascl: 2009.003
Hotan A., van Straten W., Manchester R., 2004, Publ. Astron. Soc. Pac., 21, 302
Hurley K. et al., 2020, GRB Coord. Netw., 27625, 1
Israel G. L. et al., 2016, MNRAS, 457, 3448
Israel G. L., Rea N., Zelati F. C., Esposito P., Burgay M., Mereghetti S., Possenti A., Tiengo A., 2014, Astron. Telegram, 6370, 1
Kaspi V. M., Beloborodov A. M., 2017, ARA&A, 55, 261
Kirsten F., Snelders M., Jenkins M., Nimmo K., den van Eijnden J., Hessels J., Gawronski M., Yang J., 2020a, Nat. Astron., 232
Kirsten F., Jenkins M., Snelders M., Nimmo K., Hessels J., Gawronski M., Yang J., 2020b, Astron. Telegram, 13735, 1
Kondratiev V. I. et al., 2016, A&A, 585, A128
Kothes R., Sun X., Gaensler B., Reich W., 2018, ApJ, 852, 54
Kozlova A. V. et al., 2016, MNRAS, 460, 2008
Levan A., Kouveliotou C., Fruchter A., 2018, ApJ, 854, 161
Levin L. et al., 2019, MNRAS, 488, 5251
Li C. K. et al., 2020, GRB Coord. Netw., 27679, 1
Li C. K. et al., 2021, Nat. Astron., 48
Lien A. Y. et al., 2014, GRB Coord. Netw., 16522, 1
Lin L. et al., 2020a, Nature, 587, 63
Lin L., Göğüş E., Roberts O. J., Kouveliotou C., Kaneko Y., van der Horst A. J., Younes G., 2020b, ApJ, 893, 156
Locatelli N. T. et al., 2020, MNRAS, 494, 1229
Lu W., Kumar P., Zhang B., 2020, MNRAS, 498, 1397
McMullin J. P., Waters B., Schiebel D., Young W., Golap K., 2007, in Shaw R. A., Hill F., Bell D. J., eds, ASP Conf. Ser. Vol. 376, Astronomical Data Analysis Software and Systems XVI. Astron. Soc. Pac., San Francisco, p. 127
Manchester R. N. et al., 2013, Publ. Astron. Soc. Pac., 30, e017
Mereghetti S. et al., 2020, ApJ, 898, L29
Nimmo K. et al., 2020, Astron. Telegram, 13786, 1
Offringa A. R. et al., 2014, MNRAS, 444, 606
Offringa A. R., Smirnov O., 2017, MNRAS, 471, 301
Olausen S. A., Kaspi V. M., 2014, ApJS, 212, 6
Palmer D. M., 2020, Astron. Telegram, 13675, 1
Pavlović M. Z., Urošević D., Vukotić B., Arbutina B., Göker Ü. D., 2013, ApJS, 204, 4
Pearlman A. B., Majid W. A., Prince T. A., Naudet C. J., Kocz J., 2020, Astron. Telegram, 13713, 1
Perkins S., Merry B. T M. B H., Smirnov O., 2020, AFASS 2020 Proceedings, submitted
Predehl P., Schmitt J. H. M. M., 1995, A&A, 500, 459
Ranasinghe S., Leahy D. A., Tian W., 2018, Open Phys. J., 4, 1
Ransom S., 2011, Astrophysics Source Code Library, record ascl:1107.017
Ravi V., Hallinan G., Law C. J., 2020a, Astron. Telegram, 13690, 1
Ravi V., Hallinan G., Law C. J., 2020b, Astron. Telegram, 13693, 1
Rea N., Pons J. A., Torres D. F., Turolla R., 2012, ApJ, 748, L12
Ridnaia A. et al., 2020, Nat. Astron., 30
Ruderman M. A., Sutherland P. G., 1975, ApJ, 196, 51
Sale S. E. et al., 2009, MNRAS, 392, 497
Sale S. E. et al., 2014, MNRAS, 443, 2907
Scholz P. C. C., 2020, Astron. Telegram, 13681, 404
Scholz P., CHIME/FRB Collaboration, 2020, Astron. Telegram, 13681, 1
Stamatikos M., Malesani D., Page K. L., Sakamoto T., 2014, GRB Coord. Netw., 16520, 1
Stappers B. W. et al., 2011, A&A, 530, A80
Surnis M. et al., 2020a, Astron. Telegram, 13769, 1
Surnis M. et al., 2020b, Astron. Telegram, 13799, 1
Surnis M. P., Krishnakumar M. A., Maan Y., Joshi B. C., Manoharan P. K., 2014, Astron. Telegram, 6376, 1
Surnis M. P., Joshi B. C., Maan Y., Krishnakumar M. A., Manoharan P. K., Naidu A., 2016, ApJ, 826, 184

Tavani M. et al., 2020, Astron. Telegram, 13686, 1
The CHIME/FRB Collaboration, Andersen B. Â. C.The CHIME/FRB Collaboration et al., 2020, Nature, 587, 54
Tian W.-W., Su H., Xiang F. Y., 2013, preprint (arXiv:1306.6506)
Tohuvavohu A., 2020, Astron. Telegram, 13758, 1
van Haarlem M. P. et al., 2013, A&A, 556, A2
van Straten W., Bailes M., 2011, Publ. Astron. Soc. Pac., 28, 1
Yao J. M., Manchester R. N., Wang N., 2017, ApJ, 835, 29
Younes G. et al., 2016, ApJ, 824, 138
Younes G. et al., 2017a, ApJ, 847, 85
Younes G. et al., 2017b, ApJ, 847, 85
Younes G. et al., 2021, Nat. Astron., 33
Younes G. et al., 2020b, ApJ, 904, L21
Zackay B., Ofek E. O., Gal-Yam A., 2016, ApJ, 830, 27
Zhang S. N. et al., 2020a, Astron. Telegram, 13696, 1
Zhang C. F. et al., 2020b, Astron. Telegram, 13699, 1
Zhong S.-Q., Dai Z.-G., Zhang H.-M., Deng C.-M., 2020, ApJ, 898, L5
Zhou P., Zhou X., Chen Y., Wang J.-S., Vink J., Wang Y., 2020, ApJ, 905, 99
Zhu W., Wang B., Zhou D., 2020, Astron. Telegram, 14084, 1

APPENDIX A: RADIO MONITORING CAMPAIGN

Table A1. Radio monitoring campaign of SGR J1935+2154 using the Medicina NC Telescope and the MK2 telescope at Jodrell Bank Observatory.

Telescope	T_{start} (UTC)	T_{end} (UTC)	F_{centre} (MHz)	BW (MHz)	N_{chan}	t_{samp} (μs)
Northern Cross	2020-04-30 03:00:25	2020-04-30 03:31:41	408	16	1311	138.24
Northern Cross	2020-05-02 02:23:20	2020-05-02 03:53:01	408	16	1311	138.24
Northern Cross	2020-05-03 02:20:47	2020-05-03 03:50:27	408	16	1311	138.24
Northern Cross	2020-05-04 02:15:24	2020-05-04 03:45:01	408	16	1311	138.24
Northern Cross	2020-05-05 02:33:21	2020-05-05 03:45:13	408	16	1311	138.24
Northern Cross	2020-05-06 02:07:24	2020-05-06 03:37:01	408	16	1311	138.24
Northern Cross	2020-05-12 01:43:20	2020-05-12 02:10:00	408	16	1311	138.24
Northern Cross	2020-05-14 01:36:03	2020-05-14 02:10:56	408	16	1311	138.24
Northern Cross	2020-05-15 01:39:08	2020-05-15 03:09:06	408	16	1311	138.24
Northern Cross	2020-05-16 01:27:03	2020-05-16 02:09:42	408	16	1311	138.24
Northern Cross	2020-05-17 01:23:03	2020-05-17 02:06:15	408	16	1311	138.24
Northern Cross	2020-05-18 01:19:03	2020-05-18 02:49:01	408	16	1311	138.24
Northern Cross	2020-05-19 01:15:03	2020-05-19 02:45:01	408	16	1311	138.24
Northern Cross	2020-05-20 01:10:51	2020-05-20 02:40:49	408	16	1311	138.24
Northern Cross	2020-05-21 01:06:50	2020-05-21 02:36:48	408	16	1311	138.24
Northern Cross	2020-05-22 01:03:03	2020-05-22 02:33:01	408	16	1311	138.24
Northern Cross	2020-05-23 00:59:02	2020-05-23 02:29:00	408	16	1311	138.24
Northern Cross	2020-05-24 00:55:02	2020-05-24 02:25:00	408	16	1311	138.24
Northern Cross	2020-05-25 00:51:02	2020-05-25 02:21:01	408	16	1311	138.24
Northern Cross	2020-05-26 00:47:02	2020-05-26 02:17:00	408	16	1311	138.24
Northern Cross	2020-05-27 00:43:02	2020-05-27 02:13:00	408	16	1311	138.24
Northern Cross	2020-05-28 00:39:01	2020-05-28 02:09:00	408	16	1311	138.24
Northern Cross	2020-05-29 00:35:01	2020-05-29 02:05:00	408	16	1311	138.24
Northern Cross	2020-05-30 00:31:03	2020-05-30 02:01:01	408	16	1311	138.24
Northern Cross	2020-05-31 00:27:02	2020-05-31 01:57:01	408	16	1311	138.24
Northern Cross	2020-06-01 00:23:03	2020-06-01 01:53:01	408	16	1311	138.24
Northern Cross	2020-06-02 00:19:02	2020-06-02 01:49:00	408	16	1311	138.24
Northern Cross	2020-06-03 00:15:02	2020-06-03 01:45:00	408	16	1311	138.24
Northern Cross	2020-06-04 00:11:03	2020-06-04 01:41:00	408	16	1311	138.24
Northern Cross	2020-06-05 00:07:02	2020-06-05 01:37:00	408	16	1311	138.24
Northern Cross	2020-06-07 23:56:02	2020-06-08 01:26:00	408	16	1311	138.24
Northern Cross	2020-06-08 23:52:02	2020-06-09 01:22:00	408	16	1311	138.24
Northern Cross	2020-06-09 23:48:02	2020-06-10 01:18:00	408	16	1311	138.24
Northern Cross	2020-06-11 23:42:03	2020-06-12 01:12:01	408	16	1311	138.24
Northern Cross	2020-06-12 23:37:02	2020-06-13 01:07:01	408	16	1311	138.24
MK2	2020-05-31 07:03:16	2020-05-31 07:58:16	1532	336	1538	256
MK2	2020-06-01 06:59:21	2020-06-01 07:59:16	1532	336	1538	256
MK2	2020-06-01 08:11:13	2020-06-01 08:58:40	1532	336	1538	256
MK2	2020-06-04 07:40:32	2020-06-04 08:35:00	1532	336	1538	256
MK2	2020-06-04 07:03:16	2020-06-04 07:58:16	1532	336	1538	256
MK2	2020-06-05 07:45:32	2020-06-05 08:32:30	1532	336	1538	256
MK2	2020-06-06 06:39:44	2020-06-06 07:39:44	1532	336	1538	256
MK2	2020-06-06 07:41:36	2020-06-06 08:27:36	1532	336	1538	256
MK2	2020-06-08 06:31:55	2020-06-08 07:31:55	1532	336	1538	256
MK2	2020-06-08 07:33:48	2020-06-08 08:07:48	1532	336	1538	256
MK2	2020-06-09 06:27:54	2020-06-09 07:27:54	1532	336	1538	256

Table A1 – *continued*

Telescope	T_{start} (UTC)	T_{end} (UTC)	F_{centre} (MHz)	BW (MHz)	N_{chan}	t_{samp} (μs)
MK2	2020-06-09 07:29:47	2020-06-09 08:15:47	1532	336	1538	256
MK2	2020-06-10 06:24:05	2020-06-10 07:24:05	1532	336	1538	256
MK2	2020-06-10 07:26:00	2020-06-10 08:12:00	1532	336	1538	256
MK2	2020-06-11 06:20:21	2020-06-11 07:20:21	1532	336	1538	256

APPENDIX B: MEERLICHT OBSERVATIONS

Table B1. Overview of all MeerLICHT observations on the fieldID 11744 containing the position of SGR 1935+2154, ordered by filter and date.

Image ID	Image name	Filter	Date	UT-mid	Flag	Lim. mag persistent (AB)	Lim. flux persistent (μJy)	Lim. mag transient (AB)	Lim. flux transient (μJy)
46166	ML1_20200510_022440_red	*u*	2020-05-10	02:24:41.41	Red	18.53	141.19	–	–
46172	ML1_20200510_023712_red	*u*	2020-05-10	02:37:13.13	Red	18.58	133.90	–	–
46178	ML1_20200510_024940_red	*u*	2020-05-10	02:49:41.41	Red	18.71	119.05	–	–
46948	ML1_20200515_024948_red	*u*	2020-05-15	02:49:48.48	Red	19.14	80.54	–	–
47221	ML1_20200517_024948_red	*u*	2020-05-17	02:49:48.48	Red	19.09	84.00	–	–
47384	ML1_20200518_025240_red	*u*	2020-05-18	02:52:41.41	Red	19.27	70.99	–	–
47469	ML1_20200519_025027_red	*u*	2020-05-19	02:50:27.27	Red	18.70	119.70	–	–
48101	ML1_20200521_030621_red	*u*	2020-05-21	03:06:21.21	Red	18.73	117.02	–	–
46167	ML1_20200510_022645_red	*g*	2020-05-10	02:26:46.46	Yellow	19.35	66.17	–	–
46173	ML1_20200510_023918_red	*g*	2020-05-10	02:39:19.19	Yellow	19.35	66.26	18.78	111.79
46179	ML1_20200510_025146_red	*g*	2020-05-10	02:51:47.47	Yellow	19.29	69.81	18.75	114.77
46949	ML1_20200515_025154_red	*g*	2020-05-15	02:51:54.54	Yellow	19.98	36.82	18.98	92.55
47222	ML1_20200517_025153_red	*g*	2020-05-17	02:51:53.53	Yellow	20.20	30.25	19.04	87.79
47385	ML1_20200518_025444_red	*g*	2020-05-18	02:54:45.45	Yellow	20.37	25.93	19.07	85.37
47470	ML1_20200519_025232_red	*g*	2020-05-19	02:52:32.32	Red	19.41	62.80	–	–
48102	ML1_20200521_030826_red	*g*	2020-05-21	03:08:26.26	Yellow	19.90	39.92	18.93	97.47
46168	ML1_20200510_022851_red	*q*	2020-05-10	02:28:52.52	Yellow	19.75	45.88	–	–
46174	ML1_20200510_024124_red	*q*	2020-05-10	02:41:25.25	Yellow	19.69	48.16	19.15	79.71
46180	ML1_20200510_025352_red	*q*	2020-05-10	02:53:53.53	yellow	19.59	52.94	19.06	86.17
46950	ML1_20200515_025401_red	*q*	2020-05-15	02:54:01.10	Yellow	20.43	24.35	19.41	62.61
46957	ML1_20200515_031152_red	*q*	2020-05-15	03:11:52.52	Yellow	20.33	26.81	19.37	64.83
46958	ML1_20200515_031351_red	*q*	2020-05-15	03:13:52.52	Yellow	20.33	26.74	19.37	64.77
46959	ML1_20200515_031552_red	*q*	2020-05-15	03:15:53.53	Yellow	20.31	27.38	19.37	65.08
46960	ML1_20200515_031751_red	*q*	2020-05-15	03:17:51.51	Yellow	20.30	27.55	19.35	65.89
46961	ML1_20200515_031950_red	*q*	2020-05-15	03:19:51.51	Yellow	20.22	29.53	19.31	68.44
46962	ML1_20200515_032150_red	*q*	2020-05-15	03:21:50.50	Yellow	20.41	24.92	19.40	63.12
46963	ML1_20200515_032350_red	*q*	2020-05-15	03:23:51.51	Yellow	20.35	26.23	19.38	64.36
46964	ML1_20200515_032549_red	*q*	2020-05-15	03:25:50.50	Yellow	20.14	32.01	19.25	72.18
46965	ML1_20200515_032750_red	*q*	2020-05-15	03:27:51.51	Yellow	20.36	25.99	19.38	64.15
46966	ML1_20200515_032951_red	*q*	2020-05-15	03:29:51.51	Yellow	20.31	27.19	19.36	65.17
46967	ML1_20200515_033151_red	*q*	2020-05-15	03:31:52.52	Yellow	20.25	28.78	19.34	66.94
46968	ML1_20200515_033351_red	*q*	2020-05-15	03:33:51.51	Yellow	20.38	25.55	19.39	63.47
46969	ML1_20200515_033549_red	*q*	2020-05-15	03:35:49.49	Yellow	20.40	25.11	19.40	63.13
46970	ML1_20200515_033748_red	*q*	2020-05-15	03:37:48.48	Yellow	20.25	28.94	19.33	67.30
46971	ML1_20200515_033948_red	*q*	2020-05-15	03:39:48.48	Yellow	20.36	25.95	19.39	63.79
46972	ML1_20200515_034147_red	*q*	2020-05-15	03:41:48.48	Yellow	20.28	27.94	19.37	65.07
46973	ML1_20200515_034348_red	*q*	2020-05-15	03:43:48.48	Yellow	20.12	32.45	19.28	70.35
46974	ML1_20200515_034548_red	*q*	2020-05-15	03:45:48.48	Yellow	20.21	30.02	19.32	67.61
46975	ML1_20200515_034748_red	*q*	2020-05-15	03:47:49.49	Yellow	20.16	31.21	19.32	67.94
46976	ML1_20200515_034947_red	*q*	2020-05-15	03:49:47.47	Yellow	20.11	32.83	19.29	70.13
46977	ML1_20200515_035146_red	*q*	2020-05-15	03:51:47.47	Yellow	20.15	31.61	19.31	68.28
46978	ML1_20200515_035346_red	*q*	2020-05-15	03:53:47.47	Yellow	20.16	31.20	19.32	68.20
46979	ML1_20200515_035546_red	*q*	2020-05-15	03:55:46.46	Yellow	20.15	31.67	19.31	68.32
46980	ML1_20200515_035744_red	*q*	2020-05-15	03:57:45.45	Yellow	20.17	30.96	19.32	67.97
46981	ML1_20200515_035943_red	*q*	2020-05-15	03:59:44.44	Yellow	20.12	32.55	19.30	69.34

Table B1 – *continued*

Image ID	Image name	Filter	Date	UT-mid	Flag	Lim. mag persistent (AB)	Lim. flux persistent (μJy)	Lim. mag transient (AB)	Lim. flux transient (μJy)
46982	ML1_20200515_040144_red	*q*	2020-05-15	04:01:44.44	Yellow	20.17	31.12	19.32	68.13
46983	ML1_20200515_040344_red	*q*	2020-05-15	04:03:44.44	Yellow	20.01	35.83	19.22	74.24
46984	ML1_20200515_040544_red	*q*	2020-05-15	04:05:45.45	Yellow	20.09	33.30	19.28	70.40
46985	ML1_20200515_040743_red	*q*	2020-05-15	04:07:43.43	Yellow	20.14	31.98	19.31	68.50
46989	ML1_20200515_041848_red	*q*	2020-05-15	04:18:49.49	Yellow	19.72	47.16	19.13	80.93
46990	ML1_20200515_042047_red	*q*	2020-05-15	04:20:48.48	Yellow	19.61	52.06	19.07	85.22
46991	ML1_20200515_042249_red	*q*	2020-05-15	04:22:49.49	Yellow	19.48	58.84	19.00	91.36
46992	ML1_20200515_042448_red	*q*	2020-05-15	04:24:49.49	Yellow	19.30	69.12	18.89	101.09
46993	ML1_20200515_042648_red	*q*	2020-05-15	04:26:48.48	Yellow	19.03	88.90	18.67	123.68
47223	ML1_20200517_025353_red	*q*	2020-05-17	02:53:53.53	Yellow	20.64	20.15	19.44	60.68
47229	ML1_20200517_031401_red	*q*	2020-05-17	03:14:02.20	Yellow	20.56	21.64	19.42	61.73
47230	ML1_20200517_031600_red	*q*	2020-05-17	03:16:00.00	Yellow	20.46	23.68	19.39	63.52
47231	ML1_20200517_031758_red	*q*	2020-05-17	03:17:58.58	Yellow	20.39	25.42	19.34	66.85
47232	ML1_20200517_031957_red	*q*	2020-05-17	03:19:57.57	Yellow	20.62	20.50	19.44	60.97
47233	ML1_20200517_032200_red	*q*	2020-05-17	03:22:00.00	Yellow	20.64	20.07	19.44	61.03
47234	ML1_20200517_032400_red	*q*	2020-05-17	03:24:00.00	Yellow	20.52	22.48	19.40	63.12
47235	ML1_20200517_032600_red	*q*	2020-05-17	03:26:01.10	Yellow	20.63	20.31	19.44	60.95
47236	ML1_20200517_032800_red	*q*	2020-05-17	03:28:00.00	Yellow	20.73	18.60	19.45	60.16
47237	ML1_20200517_033000_red	*q*	2020-05-17	03:30:01.10	Yellow	20.52	22.40	19.40	62.90
47238	ML1_20200517_033623_red	*q*	2020-05-17	03:36:24.24	Red	20.59	21.03	–	–
47239	ML1_20200517_033823_red	*q*	2020-05-17	03:38:23.23	Yellow	20.39	25.32	19.37	64.88
47240	ML1_20200517_034022_red	*q*	2020-05-17	03:40:23.23	Yellow	20.42	24.65	19.38	64.24
47241	ML1_20200517_034221_red	*q*	2020-05-17	03:42:22.22	Yellow	20.60	20.90	19.44	61.05
47242	ML1_20200517_034422_red	*q*	2020-05-17	03:44:23.23	Yellow	20.56	21.64	19.42	61.76
47243	ML1_20200517_034623_red	*q*	2020-05-17	03:46:23.23	Yellow	20.41	24.95	19.35	65.91
47244	ML1_20200517_034822_red	*q*	2020-05-17	03:48:23.23	Yellow	20.63	20.32	19.44	60.81
47245	ML1_20200517_035022_red	*q*	2020-05-17	03:50:23.23	Yellow	20.51	22.69	19.42	61.72
47246	ML1_20200517_035220_red	*q*	2020-05-17	03:52:21.21	Red	20.47	23.56	–	–
47247	ML1_20200517_035422_red	*q*	2020-05-17	03:54:23.23	Yellow	20.59	21.01	19.43	61.18
47248	ML1_20200517_035622_red	*q*	2020-05-17	03:56:22.22	Yellow	20.57	21.44	19.43	61.19
47249	ML1_20200517_035822_red	*q*	2020-05-17	03:58:22.22	Yellow	20.41	24.88	19.37	65.03
47250	ML1_20200517_040022_red	*q*	2020-05-17	04:00:22.22	Yellow	20.57	21.42	19.43	61.29
47251	ML1_20200517_040222_red	*q*	2020-05-17	04:02:23.23	Yellow	20.62	20.42	19.44	60.97
47252	ML1_20200517_040422_red	*q*	2020-05-17	04:04:23.23	Yellow	20.52	22.56	19.41	62.41
47253	ML1_20200517_040621_red	*q*	2020-05-17	04:06:22.22	Yellow	20.42	24.76	19.39	63.78
47254	ML1_20200517_040821_red	*q*	2020-05-17	04:08:21.21	Yellow	20.46	23.70	19.42	62.10
47258	ML1_20200517_041930_red	*q*	2020-05-17	04:19:30.30	Yellow	19.99	36.77	19.27	71.29
47386	ML1_20200518_025649_red	*q*	2020-05-18	02:56:50.50	Yellow	20.60	20.82	19.42	61.96
47390	ML1_20200518_030502_red	*q*	2020-05-18	03:05:03.30	Yellow	20.79	17.59	19.46	59.84
47391	ML1_20200518_030701_red	*q*	2020-05-18	03:07:02.20	Yellow	20.76	18.03	19.45	60.00
47392	ML1_20200518_030901_red	*q*	2020-05-18	03:09:02.20	Yellow	20.67	19.59	19.44	60.63
47393	ML1_20200518_031100_red	*q*	2020-05-18	03:11:01.10	Red	20.70	18.98	–	–
47394	ML1_20200518_031728_red	*q*	2020-05-18	03:17:29.29	Yellow	20.42	24.71	19.41	62.70
47395	ML1_20200518_031927_red	*q*	2020-05-18	03:19:27.27	Yellow	20.33	26.75	19.33	67.15
47396	ML1_20200518_032126_red	*q*	2020-05-18	03:21:26.26	Yellow	20.64	20.11	19.44	60.62
47397	ML1_20200518_032324_red	*q*	2020-05-18	03:23:24.24	Yellow	20.53	22.23	19.41	62.75
47398	ML1_20200518_032522_red	*q*	2020-05-18	03:25:22.22	Yellow	20.52	22.53	19.38	64.19
47399	ML1_20200518_032721_red	*q*	2020-05-18	03:27:21.21	Yellow	20.76	18.09	19.45	60.07
47400	ML1_20200518_032921_red	*q*	2020-05-18	03:29:22.22	Yellow	20.74	18.37	19.45	60.34
47401	ML1_20200518_033119_red	*q*	2020-05-18	03:31:20.20	Yellow	20.56	21.60	19.40	62.96
47402	ML1_20200518_033319_red	*q*	2020-05-18	03:33:19.19	Yellow	20.78	17.69	19.46	59.78
47403	ML1_20200518_033517_red	*q*	2020-05-18	03:35:18.18	Yellow	20.77	17.92	19.45	60.02
47404	ML1_20200518_033715_red	*q*	2020-05-18	03:37:15.15	Yellow	20.49	23.17	19.39	63.68
47405	ML1_20200518_033914_red	*q*	2020-05-18	03:39:14.14	Yellow	20.66	19.71	19.44	60.83
47406	ML1_20200518_034113_red	*q*	2020-05-18	03:41:13.13	Yellow	20.79	17.56	19.46	59.92
47407	ML1_20200518_034311_red	*q*	2020-05-18	03:43:12.12	Yellow	20.64	20.17	19.42	62.08
47408	ML1_20200518_034512_red	*q*	2020-05-18	03:45:13.13	Yellow	20.76	17.99	19.45	60.19
47409	ML1_20200518_034712_red	*q*	2020-05-18	03:47:13.13	Yellow	20.64	20.20	19.44	60.69
47410	ML1_20200518_034913_red	*q*	2020-05-18	03:49:13.13	Red	17.90	252.03	–	–
47411	ML1_20200518_035112_red	*q*	2020-05-18	03:51:13.13	Red	18.85	104.57	–	–
47412	ML1_20200518_035310_red	*q*	2020-05-18	03:53:10.10	Yellow	20.70	19.13	19.44	60.91
47413	ML1_20200518_035512_red	*q*	2020-05-18	03:55:12.12	Yellow	20.62	20.56	19.43	61.30
47417	ML1_20200518_040618_red	*q*	2020-05-18	04:06:18.18	Yellow	20.52	22.54	19.40	63.13

Table B1 – *continued*

Image ID	Image name	Filter	Date	UT-mid	Flag	Lim. mag persistent (AB)	Lim. flux persistent (μJy)	Lim. mag transient (AB)	Lim. flux transient (μJy)
47418	ML1_20200518_040816_red	*q*	2020-05-18	04:08:17.17	Yellow	20.56	21.71	19.42	61.80
47419	ML1_20200518_041017_red	*q*	2020-05-18	04:10:17.17	Yellow	20.56	21.60	19.43	61.54
47420	ML1_20200518_041217_red	*q*	2020-05-18	04:12:18.18	Yellow	20.53	22.19	19.42	62.20
47421	ML1_20200518_041416_red	*q*	2020-05-18	04:14:16.16	Yellow	20.54	22.00	19.42	61.83
47422	ML1_20200518_041615_red	*q*	2020-05-18	04:16:16.16	Yellow	20.31	27.30	19.38	64.44
47423	ML1_20200518_041814_red	*q*	2020-05-18	04:18:15.15	Yellow	20.34	26.43	19.38	64.20
47424	ML1_20200518_042013_red	*q*	2020-05-18	04:20:13.13	Yellow	20.23	29.25	19.35	65.80
47471	ML1_20200519_025439_red	*q*	2020-05-19	02:54:39.39	Red	18.40	159.06	–	–
47475	ML1_20200519_030259_red	*q*	2020-05-19	03:02:59.59	Red	20.11	32.85	–	–
47476	ML1_20200519_030458_red	*q*	2020-05-19	03:04:58.58	Red	20.29	27.75	–	–
47477	ML1_20200519_030658_red	*q*	2020-05-19	03:06:59.59	Yellow	20.21	29.80	19.41	62.45
47478	ML1_20200519_030857_red	*q*	2020-05-19	03:08:58.58	Yellow	20.51	22.66	19.45	60.15
47479	ML1_20200519_031059_red	*q*	2020-05-19	03:10:59.59	Yellow	20.35	26.33	19.30	69.29
47480	ML1_20200519_031256_red	*q*	2020-05-19	03:12:57.57	Red	19.81	43.45	–	–
47481	ML1_20200519_031544_red	*q*	2020-05-19	03:15:44.44	Red	19.72	47.15	–	–
47482	ML1_20200519_031742_red	*q*	2020-05-19	03:17:43.43	Red	20.51	22.66	–	–
47483	ML1_20200519_031941_red	*q*	2020-05-19	03:19:42.42	Yellow	20.46	23.84	19.35	65.84
47484	ML1_20200519_032140_red	*q*	2020-05-19	03:21:40.40	Red	20.31	27.23	–	–
47485	ML1_20200519_032339_red	*q*	2020-05-19	03:23:40.40	Red	20.67	19.56	–	–
47486	ML1_20200519_032539_red	*q*	2020-05-19	03:25:40.40	Yellow	20.70	19.14	19.28	70.28
47487	ML1_20200519_032740_red	*q*	2020-05-19	03:27:41.41	Yellow	20.16	31.33	19.42	62.12
47488	ML1_20200519_032939_red	*q*	2020-05-19	03:29:40.40	Yellow	20.13	32.19	19.25	72.59
47489	ML1_20200519_033138_red	*q*	2020-05-19	03:31:38.38	Red	19.83	42.48	–	–
47490	ML1_20200519_033336_red	*q*	2020-05-19	03:33:37.37	Red	19.52	56.52	–	–
47491	ML1_20200519_033536_red	*q*	2020-05-19	03:35:36.36	Red	19.05	86.81	–	–
47492	ML1_20200519_033735_red	*q*	2020-05-19	03:37:35.35	Red	19.90	39.98	–	–
47493	ML1_20200519_033934_red	*q*	2020-05-19	03:39:34.34	Yellow	19.99	36.76	19.41	62.45
47494	ML1_20200519_034132_red	*q*	2020-05-19	03:41:33.33	Red	20.00	36.27	–	–
47495	ML1_20200519_034332_red	*q*	2020-05-19	03:43:33.33	Red	19.67	49.33	–	–
47496	ML1_20200519_034532_red	*q*	2020-05-19	03:45:33.33	Red	19.71	47.27	–	–
47497	ML1_20200519_034735_red	*q*	2020-05-19	03:47:36.36	Red	20.07	34.01	–	–
47498	ML1_20200519_034933_red	*q*	2020-05-19	03:49:33.33	Yellow	20.43	24.37	19.45	60.15
47501	ML1_20200519_041930_red	*q*	2020-05-19	04:19:30.30	Red	15.06	3449.61	–	–
48107	ML1_20200521_031954_red	*q*	2020-05-21	03:19:54.54	Yellow	20.16	31.25	19.30	69.29
46169	ML1_20200510_023055_red	*r*	2020-05-10	02:30:56.56	Yellow	18.95	95.33	–	–
46175	ML1_20200510_024328_red	*r*	2020-05-10	02:43:29.29	Yellow	19.08	84.99	18.22	187.69
46181	ML1_20200510_025557_red	*r*	2020-05-10	02:55:58.58	Yellow	19.19	76.63	18.29	175.99
46951	ML1_20200515_025606_red	*r*	2020-05-15	02:56:06.60	Yellow	19.72	46.85	18.43	154.13
47224	ML1_20200517_025556_red	*r*	2020-05-17	02:55:56.56	Yellow	19.78	44.34	18.41	157.72
47472	ML1_20200519_025643_red	*r*	2020-05-19	02:56:43.43	Red	18.66	124.89	18.46	149.83
46170	ML1_20200510_023300_red	*i*	2020-05-10	02:33:01.10	Yellow	18.79	110.50	–	–
46176	ML1_20200510_024532_red	*i*	2020-05-10	02:45:33.33	Yellow	18.79	111.03	18.22	187.69
46182	ML1_20200510_025802_red	*i*	2020-05-10	02:58:03.30	Yellow	18.91	99.28	18.29	175.99
46952	ML1_20200515_025811_red	*i*	2020-05-15	02:58:11.11	Yellow	19.32	67.76	18.43	154.13
47225	ML1_20200517_025802_red	*i*	2020-05-17	02:58:02.20	Yellow	19.25	72.75	18.41	157.72
47388	ML1_20200518_030049_red	*i*	2020-05-18	03:00:50.50	Yellow	19.49	58.23	18.46	149.83
47473	ML1_20200519_025848_red	*i*	2020-05-19	02:58:48.48	Red	18.06	216.36	–	–
46171	ML1_20200510_023505_red	*z*	2020-05-10	02:35:06.60	Yellow	17.92	246.81	–	–
46177	ML1_20200510_024738_red	*z*	2020-05-10	02:47:39.39	Yellow	17.86	259.62	17.30	436.24
46183	ML1_20200510_030007_red	*z*	2020-05-10	03:00:08.80	Yellow	17.98	233.71	17.37	409.28
46953	ML1_20200515_030018_red	*z*	2020-05-15	03:00:18.18	Yellow	18.20	191.12	17.46	376.41
47226	ML1_20200517_030008_red	*z*	2020-05-17	03:00:08.80	Yellow	18.04	220.28	17.38	406.98
47389	ML1_20200518_030256_red	*z*	2020-05-18	03:02:57.57	Yellow	18.17	196.21	17.44	385.04
47474	ML1_20200519_030054_red	*z*	2020-05-19	03:00:54.54	Red	17.56	342.28	–	–

Notes. All exposures were 60 s in duration. Limiting magnitudes/fluxes for the detection of persistent sources are at a S/N of 5σ; limiting magnitudes/fluxes for the detection of transient sources are at a transient peak significance level (Scorr value) of 6. Red flagged images do not get processed for transient detections.

[1]*Centre for Astrophysics and Supercomputing, Swinburne University of Technology, Mail 74 PO Box 218, Hawthorn, VIC 3122, Australia*
[2]*ARC Centre of Excellence for Gravitational Wave Discovery (OzGrav), Australia*
[3]*ASTRON, Netherlands Institute for Radio Astronomy, Oude Hoogeveensedijk 4, NL-7991 PD, Dwingeloo, the Netherlands*
[4]*INAF-Istituto di Radio Astronomia, via Gobetti 101, I-40129 Bologna, Italy*
[5]*Department of Physics and Electronics, Rhodes University, PO Box 94, Grahamstown 6140, South Africa*
[6]*South African Radio Astronomy Observatory, Black River Park, 2 Fir Street, Observatory, Cape Town 7925, South Africa*
[7]*INAF-Osservatorio Astronomico di Cagliari, via della Scienza 5, I-09047 Selargius (Cagliari), Italy*
[8]*Jodrell Bank Centre for Astrophysics, Department of Physics and Astronomy, University of Manchester, Manchester M13 9PL, UK*
[9]*Anton Pannekoek Institute for Astronomy, University of Amsterdam, Science Park 904, NL-1098 XH Amsterdam, the Netherlands*
[10]*Max-Planck-Institut für Radioastronomie, Auf dem Hügel 69, D-53121 Bonn, Germany*
[11]*LESIA, Observatoire de Paris, Université PSL, CNRS, Sorbonne Université, Université de Paris, 5 place Jules Janssen, F-92195 Meudon, France*
[12]*Department of Astrophysics/IMAPP, Radboud University, PO 9010, NL-6500 GL, Nijmegen, the Netherlands*
[13]*Inter-University Institute for Data Intensive Astronomy and Department of Astronomy, University of Cape Town, Private Bag X3, Rondebosch 7701, South Africa*
[14]*South African Astronomical Observatory, PO Box 9, 7935 Observatory, Cape Town, South Africa*
[15]*Astrophysics, Department of Physics, University of Oxford, Keble Road, Oxford OX1 3RH, UK*
[16]*INAF OAS Bologna, Via P. Gobetti 101, I-40129 Bologna, Italy*
[17]*Astro Space Centre, Lebedev Physical Institute, Russian Academy of Sciences, Profsoyuznaya Str. 84/32, Moscow 117997, Russia*
[18]*Leiden Observatory, Leiden University, P.O. Box 9513, NL-2300 RA Leiden, the Netherlands*
[19]*CSIRO Astronomy and Space Science, Australia Telescope National Facility, PO Box 76, Epping, NSW 1710, Australia*
[20]*Institute of Space Sciences and Astronomy (ISSA), University of Malta, Msida, MSD 2080, Malta*
[21]*IAU-Office For Astronomy for Development, PO Box 9, 7935 Observatory, Cape Town, South Africa*
[22]*Center for Interdisciplinary Exploration and Research in Astrophysics (CIERA), Northwestern University, 1800 Sherman Ave, Evanston, IL 60201, USA*
[23]*Arecibo Observatory, Route 625 Bo. Esperanza, Arecibo, PR 00612, USA*
[24]*Department of Physics, McGill University, 3600 University Street, Montréal, QC H3A 2T8, Canada*
[25]*McGill Space Institute, McGill University, 3550 University Street, Montréal, QC H3A 2A7, Canada*
[26]*Universitä degli Studi di Cagliari, Dip di Fisica, S.P. Monserrato-Sestu Km 0,700, I-09042 Monserrato (CA), Italy*
[27]*Dipartimento di Fisica e Astronomia, Universitá di Bologna, Via Gobetti 93/2, I-40129 Bologna, Italy*
[28]*INAF/IAPS, via del Fosso del Cavaliere 100, I-00133 Roma (RM), Italy*
[29]*Universitä degli Studi di Roma 'Tor Vergata', via della Ricerca Scientifica 1, I-00133 Roma (RM), Italy*

This paper has been typeset from a TEX/LATEX file prepared by the author.